AD-A276061

# INFRARED FIBER OPTIC DIAGNOSTIC OBSERVATIONS OF SOLID PROPELLANT COMBUSTION

Final Report

DTIC
ELECTE
FEB 2 5 1994
A

Prepared by

J. Wormhoudt, P. L. Kebabian, and C.E. Kolb
Center for Chemical and Environmental Physics
Aerodyne Research, Inc., 45 Manning Road, Billerica, MA 01821

DTIC Q

October 1993

Best Available Copy

# REPORT DOCUMENTATION PAGE

Public reporting burden for this collection of information is estimated to average 1 hour per response, including the time for reviewing instructions, searching existing data sources, gathering and maintaining the data needed, and completing and reviewing the collection of information. Send comments regarding this burden estimate or any other aspect of this collection of information, including suggestions for reducing this burden, to Washington Headquarters Services, Directorate for Information Operations and Reports, 1215 Jefferson Davis Highway, Suite 1204, Arlington, VA 22202-4302, and to the Office of Management and Budget, Paperwork Reduction Project (0704-0188), Washington, DC 20503

| 1. AGENCY USE ONLY (Leave blank) | 2. REPORT DATE 30 November 1993 | 3. REPORT TYPE AND DATES COVERED Final Report, 1/21/91-9/30/93 |
|---|---|---|

| 4. TITLE AND SUBTITLE Infrared Fiber Optic Diagnostic Observations of Solid Propellant Combustion | 5. FUNDING NUMBERS DAAL03-91-C-0068 |
|---|---|

**6. AUTHOR(S)**

J. Wormhoudt, P.L. Kebabian, and C.E. Kolb

| 7. PERFORMING ORGANIZATION NAME(S) AND ADDRESS(ES) Aerodyne Research, Inc. 45 Manning Road Billerica, MA 01821 | 8. PERFORMING ORGANIZATION REPORT NUMBER ARI-RR-1029 |
|---|---|

| 9. SPONSORING/MONITORING AGENCY NAME(S) AND ADDRESS(ES) U. S. Army Research Office P. O. Box 12211 Research Triangle Park, NC 27709-2211 | 10. SPONSORING/MONITORING AGENCY REPORT NUMBER ARO 28103.1-CH-S |
|---|---|

**11. SUPPLEMENTARY NOTES**

The view, opinions and/or findings contained in this report are those of the author(s) and should not be construed as an official Department of the Army position, policy, or decision, unless so designated by other documentation.

| 12a. DISTRIBUTION/AVAILABILITY STATEMENT Approved for public release; distribution unlimited. | 12b. DISTRIBUTION CODE |
|---|---|

**13. ABSTRACT (Maximum 200 words)**

We report on work to develop and demonstrate a diagnostic technique using infrared fiber optics to probe the decomposition processes in burning gun propellant strands. The experiments reported here involve measuring the absorption across an open gap between two embedded fibers as it fills with gaseous decomposition products. Spectroscopic detection is achieved using pairs of bandpass filters. The absorption record can be correlated with readings from embedded thermocouples and with a high resolution video recording of the burn. We have observed $N_2O$, a decomposition product of RDX, evolving into the observation volume. The $N_2O$ appearance is often an abrupt event. Coupled with evidence that it can occur while the observation region is relatively cool and far from the burning surface (observed in cases involving burning at 6 atm pressure), these observations suggest hypotheses concerning the physical processes in the condensed phases of this propellant, hypotheses including the development of pressurized voids or matrix-trapped bubbles which can release decomposition gases into the unburnt propellant through suddenly opening cracks. The appearance of $N_2O$ after the temperature record suggests that melting and decomposition of RDX have begun (observed in 1 atm cases) implies that $N_2O$ formation is indeed not an initial step in RDX decomposition under our conditions.

| 14. SUBJECT TERMS solid propellant combustion infrared fiber optic absorption diagnostic | | | 15. NUMBER OF PAGES 41 |
|---|---|---|---|
| | | | 16. PRICE CODE |

| 17. SECURITY CLASSIFICATION OF REPORT UNCLASSIFIED | 18. SECURITY CLASSIFICATION OF THIS PAGE UNCLASSIFIED | 19. SECURITY CLASSIFICATION OF ABSTRACT UNCLASSIFIED | 20. LIMITATION OF ABSTRACT UL |
|---|---|---|---|

NSN 7540-01-280-5500

# TABLE OF CONTENTS

# LIST OF FIGURES

LIST OF FIGURES (Continued)

# LIST OF TABLES

# 1.0 INTRODUCTION

Recently, a study group sponsored by the Army Research Office developed and published an overall basic research plan to guide advanced research on key nitramine propellant ignition and combustion issues which must be addressed to allow the systematic exploitation of this exciting class of energetic materials.[1] Subsequent workshops organized by the Office of Naval Research and the JANNAF Combustion Subcommittee on Nitramine Propellants have further refined the outstanding issues. The work reported here is a response to a need identified by all these groups, the development of new diagnostic techniques to monitor the progress of decomposition and ignition kinetics in the condensed phase.

There have been very few direct measurements of condensed phase decomposition in burning gun propellants. Our technique, motivated by recent advances in electro-optical material, is the use of embedded optical fibers. We have begun by investigating the use of infrared-transmitting fibers in a direct absorption experiment, in which a gap between a pair of embedded fibers may allow spectroscopic detection of decomposition products within a strand of solid propellant.

Although ours is the first spectroscopic investigation in the solid phase of burning propellants, it has benefitted from a number of related research programs (a recent comprehensive review of experimental and theoretical work is found in Reference 2). Infrared absorption has been used to study the decomposition of propellant ingredients, including the nitramines HMX and RDX[3-7] as well as other materials.[8] These studies all used Fourier transform infrared spectrometers to measure the changing absorption of thin films of the materials as they underwent rapid heating[3-6] or photolysis by an ultraviolet lamp.[7] In particular, the spectra reported in Reference 3, in which the absorption bands of $N_2O$ and $CO_2$ can be seen as these gases accumulate in bubbles forming in confined thin films of HMX and RDX, did much to encourage us in our approach. Other programs providing useful information have included the work by Miller on embedding fine-wire thermocouples in burning propellant strands,[9] the ongoing work at Sandia National Laboratories involving infrared spectra of heated RDX films,[10] and work by Litzinger and co-workers on mass spectrometer sampling of laser-heated propellant samples.[11]

## 2.0 EXPERIMENTAL TECHNIQUES

Our goal was to develop a technique of fast-response spectral infrared fiber probing of burning propellant strands, and demonstrate it in mechanism studies of condensed phase processes in nitramine propellant combustion. In early stages of this work, we focused on observing chemical changes in solid propellant by infrared absorption, embedding a pair of fibers separated by a sliver of propellant. We will not report on that work here, but instead confine our discussion to a second experimental configuration which has been much more successful. In these experiments, the gap between fibers (inside the propellant strand) was lengthened to 0.2 to 0.5 cm and left empty. This air-filled cavity or observation volume could then fill with gas-phase decomposition products as the flame front approached. Observations including when, how fast, and to what levels it was filled could be used to support hypotheses as to the source of the decomposition gases.

Previous studies,[1-3,11] indicated that nitramine propellant ingredients such as RDX may decompose into a number of gaseous species including $N_2O$, $H_2CO$, $NO_2$, HCN, $H_2O$, NO, and $CO_2$. The fiber length used here of about 1 m means the transmission band of the fiber matches the response curve of the detectors, both extending from less than 2 to about 5 μm. This allows sensitive detection of $N_2O$ in the $v_3$ band around 4.7 μm, as well as $CO_2$ in the band around 4.3 μm, $H_2CO$ around 3.5 μm and, with a laser source, NO around 5.2 μm. Of these, $N_2O$ was chosen as the first example because, of those species expected to give strong infrared absorption signals with the first version of our apparatus, it was of greatest interest for the definition of chemical mechanisms of decomposition. Extensions of optical fiber probe techniques to other visible and infrared wavelengths to quantify other potential decomposition species including $NO_2$ are being explored in a follow-on effort.

A schematic diagram of the experiment reported here is illustrated in Figure 1. The chopping wheel modulates the light from an infrared source (a globar), and so the transmitted signal, at approximately 2000 Hz. The light is focused onto a fluoride glass optical fiber (Infrared Fiber Systems) of 200 μm nominal diameter. The propellant strand is mounted inside a high pressure strand burner (shown in Figure 2). The embedded optical fibers pass through the baseplate of the strand burner, as do leads connecting a variac to a V-shaped segment of nichrome wire pressed against the top of the strand to provide ignition. In the observations reported here, the gaps between the source and detector fibers are in the 0.2 to 0.5 cm range. Light collected by the fiber on the detector side is divided by a 50/50 beamsplitter and passes through a pair of narrow band infrared interference filters before being focused onto InSb infrared detectors.
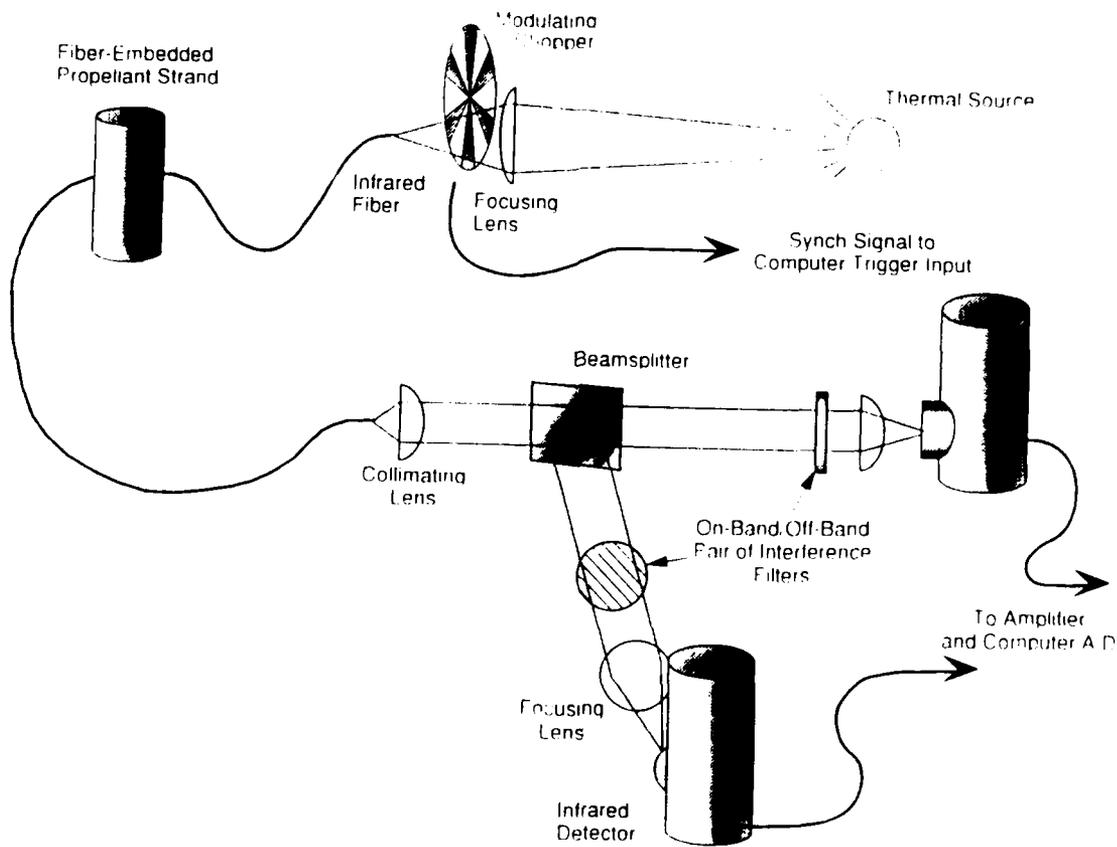
Figure 1. Schematic Drawing of Infrared Fiber Optic Absorption Experiment.

A data acquisition computer reads a signal point from each infrared detector at each on and off point of the chopper. Computer data acquisition for each chopper cycle is triggered by the synchronization signal from the commercial chopper controller. The signals from the infrared detectors and pre-amplifiers pass through buffer amplifiers to minimize the effects of the analog to digital conversion. This also allows optimization of the time response of the signal, so the single data point the computer reads is representative of the entire half-cycle of the chopper.

The strand burner shown in Figure 2 is a copy of a device in use at the U.S. Army Research Laboratory, Aberdeen Proving Ground, with some modifications to accommodate fiber optics. The only propellant studied to date has been XM39, composed of 75% RDX and 25% binder. Its detailed composition is shown in Table 1. Experiments were performed at 2 pressures, 1 and 6 atm. Although both pressures are far from those encountered in rocket combustion chambers, let alone in cannon shells, it turns out that the variation in burning rate between the two pressure regimes is large enough to give qualitatively different observations and hence useful information.

PRESSURIZATION/
EXHAUST PORT

OBSERVATION
WINDOWS

PROPELLANT
STRAND

FIBER
OPTIC

INPUT LIGHT

TRANSMITTED
LIGHT TO
DETECTORS

SHIELD GAS FLOWS

COMBUSTION GAS FLOW
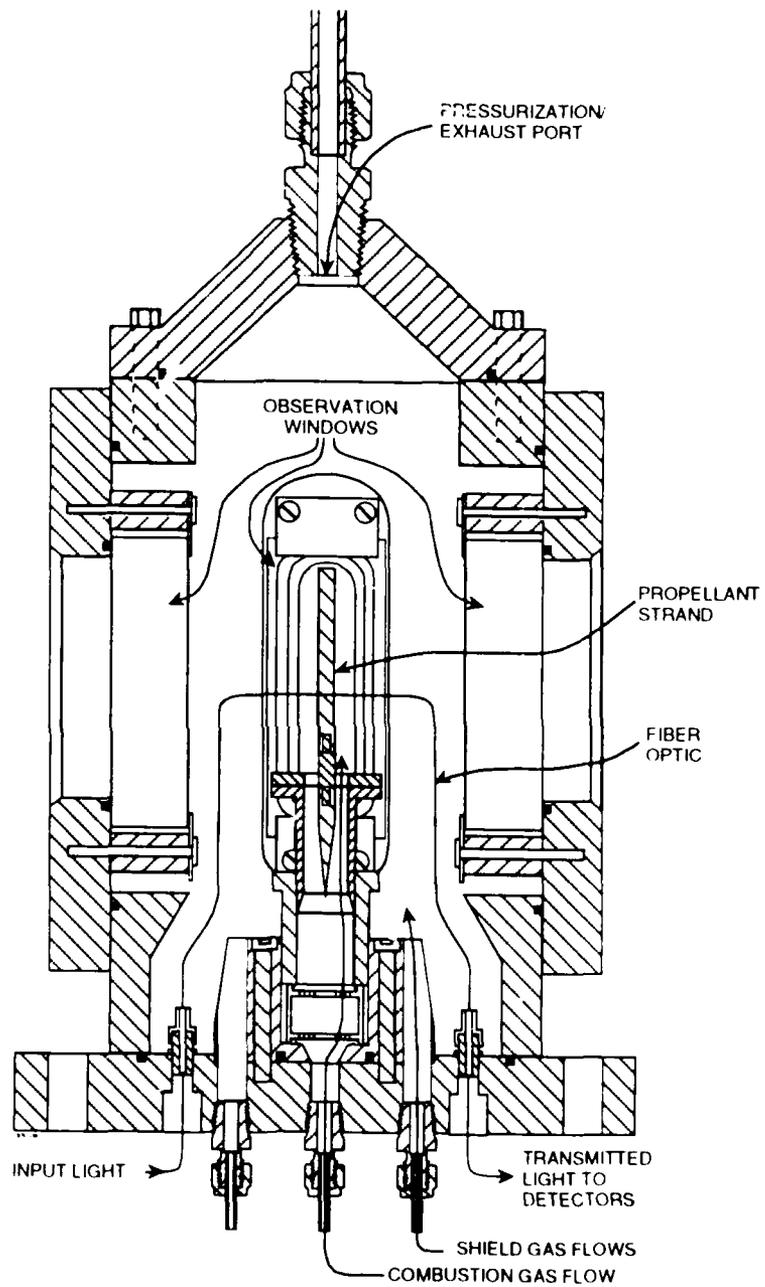
Figure 2. Cross-Section of Strand Burner.

4

Table 1. Composition of XM39 Propellant

| Component Name | Chemical Formula | Mass Fraction | Melting Point |
|---|---|---|---|
| RDX (5 micron) | $C_3H_6N_6O_6$ | 0.76 | 190 °C |
| Cellulose Acetate Butyrate (CAB) | $C_{15}H_{22}O_8$ | 0.12 | 215-225 °C |
| Nitrocellulose (NC) | $C_6H_{7.55}O_5(NO_2)_{2.45}$ | 0.04 | 160-170 °C |
| Acetyl Triethyl Citrate (ATC) | $C_{14}H_{22}O_8$ | 0.076 | (B. P. 132 °C) |
| Ethyl Centralite (EC) | $C_{17}H_{20}ON_2$ | 0.004 | 72 °C |

XM39 will not burn in an inert atmosphere at 1 atm, so we used secondary combustion of the gaseous decomposition products with air to support the primary combustion of the solid propellant. A combination of nitrogen addition to the air and a large enough flow velocity around the strand was used to prevent burning down the side of the strand. At atmospheric pressure, we used a gas flow through the central inlet composed of 235 STP cm$^3$/s air and 40 STP cm$^3$/s N$_2$, for a gas velocity around the strand of roughly 3.5 cm/s. At 6 atm, the air and N$_2$ flows were increased to 2470 and 825 STP cm$^3$/s, respectively, changing the velocity of the gas flow around the strand to around 7 cm/s. Under these gas flow conditions, the strand burns with a roughly flat melt layer and a slightly concave burning surface. From measurements discussed below, we found propellant burning rates of about 0.015 cm/s at 1 atm, and 0.041 cm/s at 6 atm.

A high-resolution video system is used to record each burn. The beginning of data collection is accompanied by a computer signal to the video recorder which starts its time clock. With a second lens, the video camera is also used as a microscope during fiber insertion.

The fibers are inserted between two sections of a propellant strands, cut with a diamond saw. The fiber insertion procedure begins with the formation of a groove in both propellant pieces. The strand segment is placed in a hole in a warmed metal block. At the bottom of the hole is a wire stretched across its diameter. The wire thickness is chosen so that heavy pressure on the strand leaves the proper indentation on its face. Using a knife, grooves for thermocouples (0.0127 cm diameter, chromel-alumel) are cut to within approximately 0.1 cm of the fiber groove. Then, after

the fibers are positioned in the groove, they are pressed into the groove using the top propellant piece, the thermocouples are inserted, and both fibers and thermocouples are secured inside the strand with cyanoacrylate adhesive at the entry points. Figure 3 illustrates the technique. The reassembled strand has a cylindrical cavity or observation volume with a diameter of about 0.02 cm and a length of 0.2 to 0.5 cm, with thermocouple junctions on one or both sides of it, a few fiber diameters outside the wall of the cavity and from 0.005 cm to 0.02 cm below the plane containing the fiber.
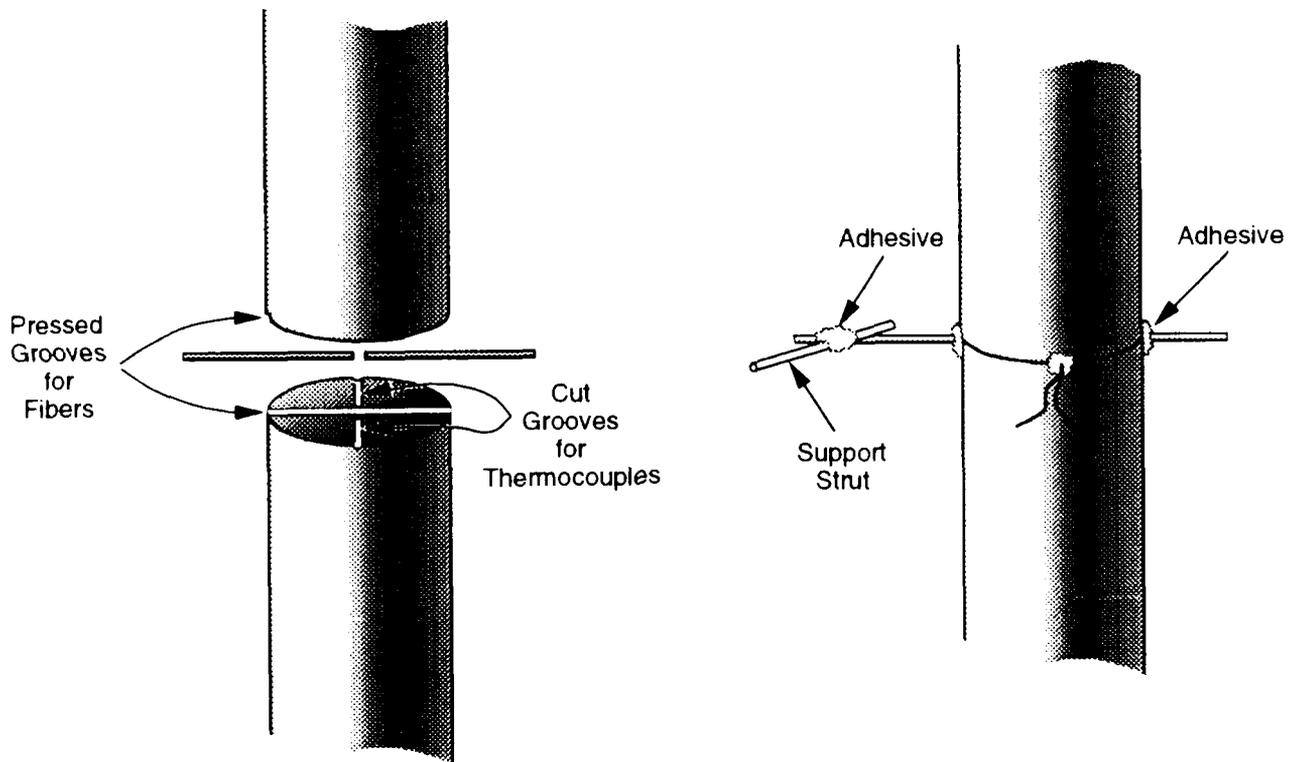


Figure 3. Fiber Insertion Procedure.

# 3.0 EXPERIMENTAL ANALYSIS

## 3.1 Nitrous Oxide Quantification

The 50% transmission points of the filter used to detect $N_2O$ were at about 2185 and 2238 cm$^{-1}$, while those of the reference filter were 2093 and 2196 cm$^{-1}$. Since the half-height points of the $N_2O$ absorption band are at around 2184 and 2254 cm$^{-1}$, it is clear not only that the $N_2O$ filter closely overlaps the $N_2O$ band, but also that the reference filter detector will be somewhat sensitive to the presence of $N_2O$ in the absorption path. Initially, we simply included this sensitivity in the analysis relating the ratio of the two filter intensities to $N_2O$ mole fractions. In later experiments a short cell filled with one atmosphere of $N_2O$ was placed in front of the reference filter, so that light reaching the reference detector only had wavelengths which are not absorbed by $N_2O$, thus eliminating the sensitivity.

The filter responses were calibrated computationally, using Fourier transform infrared spectrometer measurements of the bandpass filter transmission curves, and $N_2O$ spectral absorbance values derived from the HITRAN absorption line database[12]. Although it was checked against observations made by filling the strand burner with a range of pressures of $N_2O$ while the gap between fibers was still uncovered, the computational calibration is the primary basis for the observed mole fractions reported here, because it most easily allows us to take into account changes in the in-band absorption due to changes in line strengths and widths with temperature.

The transmitted intensity signals are obtained from computer files of the detector outputs by differencing each pair of chopper-open and chopper-closed values. These intensity records are then averaged— an average of 63 pairs of points yields a 30 Hz data record, and for noisier data 10 Hz or 5 Hz averages are used. After the fiber has burned through, the remaining data stream is averaged to give a zero level which is subtracted from each detector signal before the ratio is taken. The value of this ratio, relative to its value before ignition, gives a fractional transmission in the $N_2O$ band. It is compared with the calibrations described above to directly yield the product of the pathlength and the $N_2O$ number density and, with further assumptions, the $N_2O$ mole fraction.

## 3.2 Flame Front Position Measurement

The video record of each burn was examined to yield a record of the position of the burning surface, synchronized with the computer records of infrared transmission and thermocouple temperatures. Flame front positions were typically measured at intervals of one second or more

with a time uncertainty of less than the frame period of 1/30 s and a position uncertainty of about 0.02-0.03 cm (the raster spacing for the range of image magnifications used). These position histories typically exhibit quite steady burn rates. Some burns do have irregularities near the fiber insertion point. These irregularities may in some cases be due to a change in the burn rate across the entire face of the propellant strand, but many apparent irregularities are due to difficulties in seeing the center of the strand, such that the point chosen to represent the burning surface is on a front edge. An edge region may burn slower or faster as the fiber insertion point is approached, because of the heat transfer and air flow perturbations of the fibers, thermocouples, adhesive, and the cut through the strand.

There could be, therefore, a difference of as much as 0.1 cm in some cases between the position in the transcription of the video record and the actual distance from the flame front in the center of the strand to the fiber insertion plane. To give a measure of how much these differences affect ensemble averages of a quantity such as the fiber-to-flame-front distance when $N_2O$ first appears in the observation volume, we will report this distance based both on the point-by-point video record, and on a least squares fit to the entire position history. The two positions agree far from the fiber insertion point, and if the burning rate of the center of the strand were more regular than that of the edges, we might expect the linear fit to give somewhat more reliable fiber-to-flame-front distances.

## 3.3 Propellant Temperatures Measurements

As noted above, the thermocouples had 0.0127 cm wire diameters, and the diameter of the bead at the junction is more than double this value. However, we are convinced that the major source of uncertainty in the thermocouple readings is not this relatively large size or issues of good thermal contact with the propellant or heat transfer out through the thermocouple, but rather the (occasional) irregularity in the burning surface in the vicinity of the fibers. As discussed above, the burning surface far from the fibers is relatively perpendicular to the axis of the strand and is slightly concave. As the flame burns through the cut in the strand and around the adhesive beads on the strand surface which secure the fibers and thermocouples, the slope of the burning surface can become larger, such that the thermocouple bead could be in a warmer or colder region of propellant than the fiber gap of order 0.1 cm away from it. It should also be said, though, that in our burns in which two thermocouples were inserted, the two temperature traces agreed well.

# 4.0 EXPERIMENTAL RESULTS

## 4.1 Example Data Traces

Figures 4 and 5 present examples of the data traces near the time of $N_2O$ appearance for the two pressure regimes studied (1 and 6 atm). The figures show the two detector intensities (both normalized to one at their maximum values), their ratio, the embedded thermocouple temperature, and the two measures of distance between the burning surface and the fiber. In both cases, the $N_2O$ (as indicated by the drop in the ratio of detector intensities) appears and reaches a fairly constant level in a time between 0.1 and 0.2 s. It must be pointed out that the two pressures differ in how often this abrupt $N_2O$ appearance is observed, since it is seen in 5 of 6 cases at 6 atm, while in 5 of 7 1 atm cases the $N_2O$ appears over times ranging from 0.3 to 2.0 s.

If we assume that the $N_2O$ is at the temperature of the embedded thermocouples (as mentioned above, an assumption with some uncertainty, but we have no better source of gas temperature information) we can use the known absorption path lengths to calculate $N_2O$ mole fractions, which are 0.05 for the 6 atm case in Figure 4 and 0.18 for the 1 atm case in Figure 5. If we make the conservative assumption that the ranges of thermocouple temperatures at which $N_2O$ appears (discussed below) represent the uncertainty in the temperature of the $N_2O$ in the observation volume, then from our precalculated filter calibration factors we find that at 1 atmosphere this translates into a relative uncertainty of less than $\pm 0.3$ in $N_2O$ mole fraction, while at 6 atm, the relative uncertainties in $N_2O$ vary within the range of $\pm 0.05$ to $\pm 0.20$ as the transmission varies from 0.8 to 0.2.

After its initial abrupt appearance, the $N_2O$ level (and the infrared transmission through the observation volume) is maintained for an average of about 0.4 s in the 6 atm cases and for between 1 and 2 s in the 1 atm cases (in the 1 atm cases with more gradual $N_2O$ appearance the time between first appearance and loss of transmission is also on the order of 1 s). We will report two time segments for the abrupt appearance cases, referring to them as fill times and steady state times, in spite of the facts that in other cases they are part of a continuous event of $N_2O$ appearance in the observation volume, and that $N_2O$ absorption after the initial fill is only relatively constant. On this latter point, we can note that in Figure 4 a change in $N_2O$ temperature from 100 to 140 °C (following the rising thermocouple reading) would be expected to cause the transmission to increase from 0.74 to 0.78— in fact, if anything it decreases, suggesting that the $N_2O$ mole fraction is increasing in the observation volume, although at a much slower rate.

After some time at a fairly steady $N_2O$ level, a second relatively abrupt event brings the transmission to zero. It can be seen in this region that the absolute transmission can drop by an order of magnitude while the ratio of the two transmissions remains constant. Therefore, the experiment is concluded by events whose effects on the transmission have no spectral dependence over the range of the bandpass filters, such as misalignment of the fibers or entry of liquid into the observation path.

Figures 4 and 5 exemplify a second difference between the two pressure regimes, that the appearance of the $N_2O$ takes place in different temperature ranges — at under 100 °C in the 6 atm example, but when the thermocouple reading is about 250 °C in the 1 atm case. Finally, the values of fiber insertion plane to burning surface distance at $N_2O$ appearance seen in the two figures are in fact representative of the range seen in all cases. At 6 atm, interpolation in the point-by-point record gives a distance of 0.12 cm while using the linear fit through all position points gives a distance of 0.13 cm. At 1 atm, the two distance values are 0.21 and 0.24 cm.

As mentioned above, Figure 4 is representative of the majority of the 6 atm cases, but Figure 5 is not representative of most of the 1 atm cases, which instead look like the example in Figure 6. Here, the $N_2O$ appears gradually, over a time period of at least a second, before transmission is lost. The temperature and flame-to-fiber distance ranges where transmission is lost are not significantly different from those seen in the abrupt cases.

The 1 atm cases, with a much smaller change in transmission for the same $N_2O$ mole fraction, usually had a signal-to-noise level like that shown in Figure 6. Without fitting a smooth curve to the observed transmission it is difficult to see that there is a systematic decrease in transmission corresponding to $N_2O$ appearance. The one 1 atm case in which $N_2O$ appearance is easily visible, shown in Figure 7, is also one of two cases to show a second phenomenon: the subsequent disappearance of $N_2O$, again on the relatively slow time scale of a few seconds.

This phenomenon was also seen in the 6 atm case shown in Figure 8. Once again, the $N_2O$ both appears and disappears on a relatively slow time scale. Furthermore, a second, more abrupt and higher concentration appearance of $N_2O$ may occur just before transmission loss. (Note that the data set of Figure 8 is clearly one of those taken before the addition of the $N_2O$ gas filter in front of the reference detector, since both detector signals respond to the appearance of $N_2O$.) The cases in Figures 7 and 8 share two characteristics which may help to explain why only they show
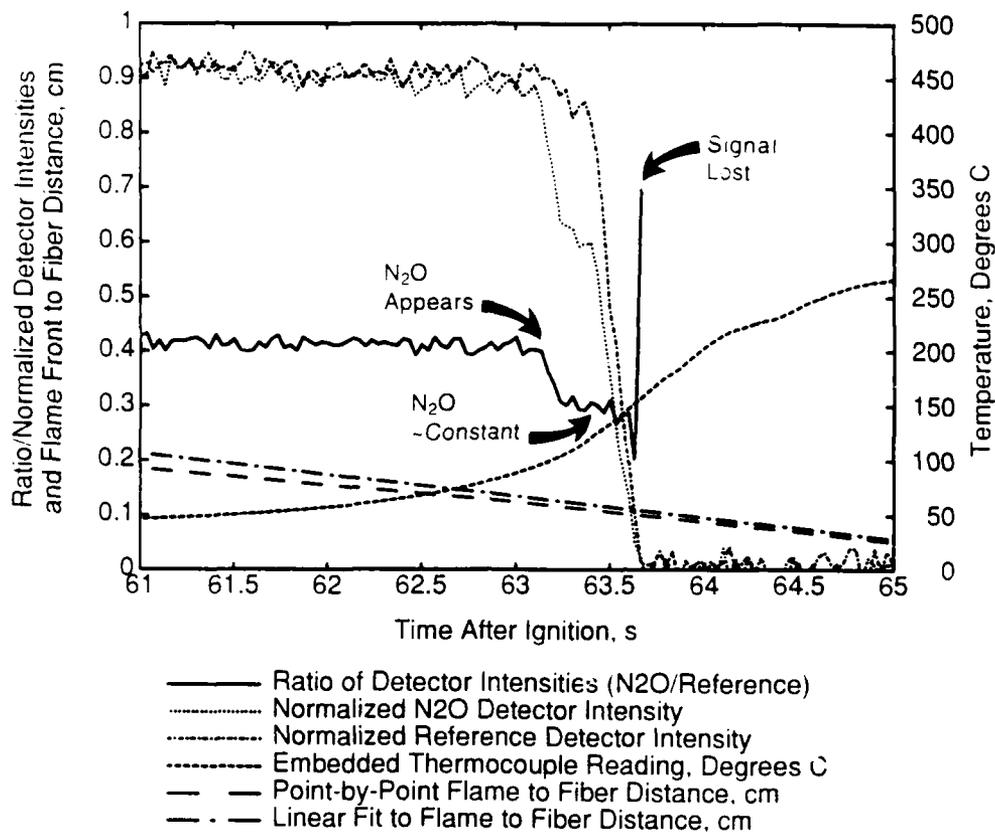
Figure 4. Example Data for XM39 Burning at 6 atm Pressure.

$N_2O$ disappearance: they both maintained good infrared transmission for several seconds after $N_2O$ appearance, and their thermocouple temperature readings in the steady state region were the highest in each pressure set.

In other experiments, we found that the fluoride glass fibers can maintain high transmission even when heated well above the softening point. The loss of transmission depends on mechanical deformation, not on the fiber temperature per se. In the strand experiments, another factor would be misalignment of the two fibers once the surrounding material has melted. Thus, with improved support for the fiber it might be possible to obtain observations such as those in Figure 7 and 8 routinely.

The final example, in Figure 9, was done to add support to the hypothesis that abruptly appearing $N_2O$ is not evolved from the walls of the observation volume but arrives from regions
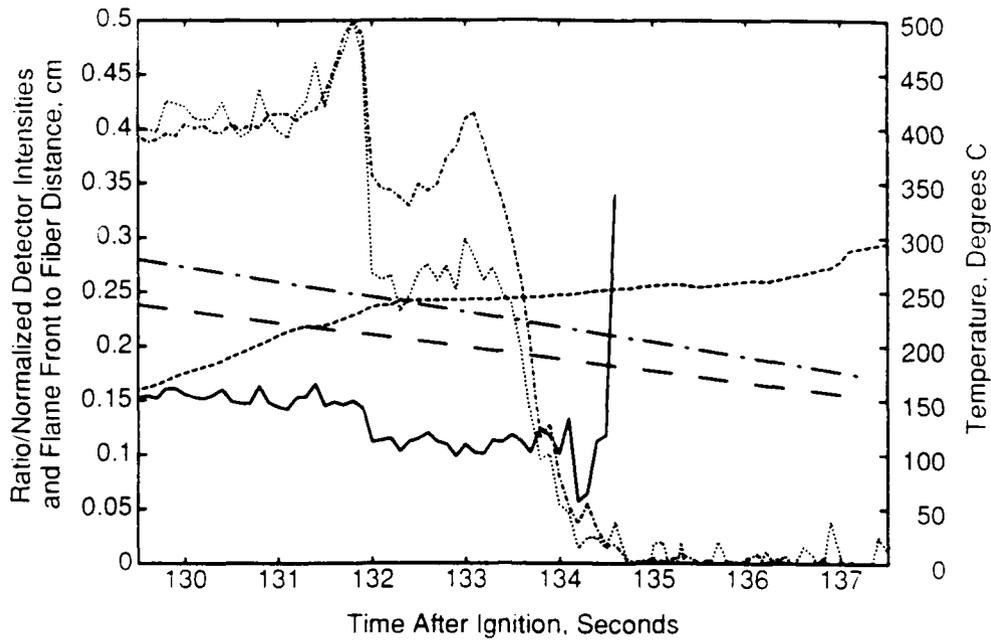
Figure 5. Example Data for XM39 Burning at 1 atm Pressure. (Same key as Figure 4). In this run, an $N_2O$ gas filter cell was not used, so both detectors respond to $N_2O$.
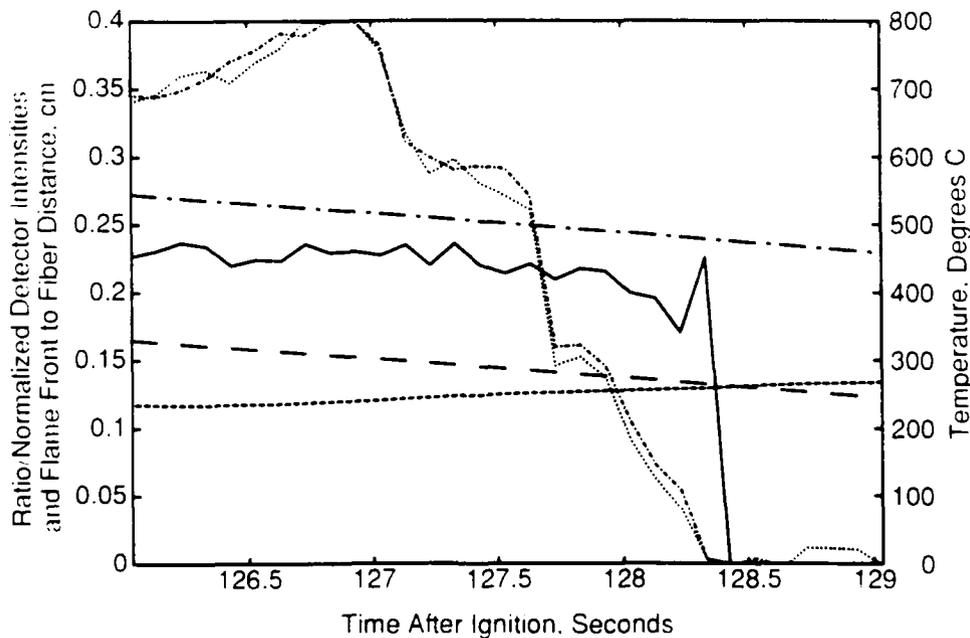


Figure 6. Example Observations for XM39 Burning at 1 atm Pressure, Showing Slower $N_2O$ Evolution. (Same key as Figure 4.)
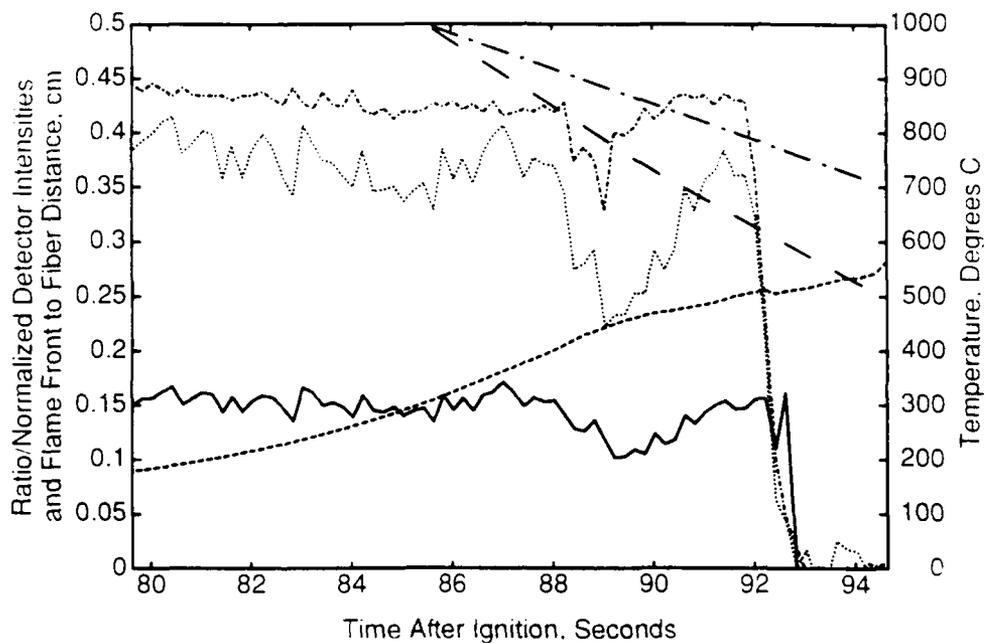
Figure 7. XM39 Burning at 1 atm Pressure. Showing Slow Appearance and Disappearance of N₂O. (Same key as Figure 4.)
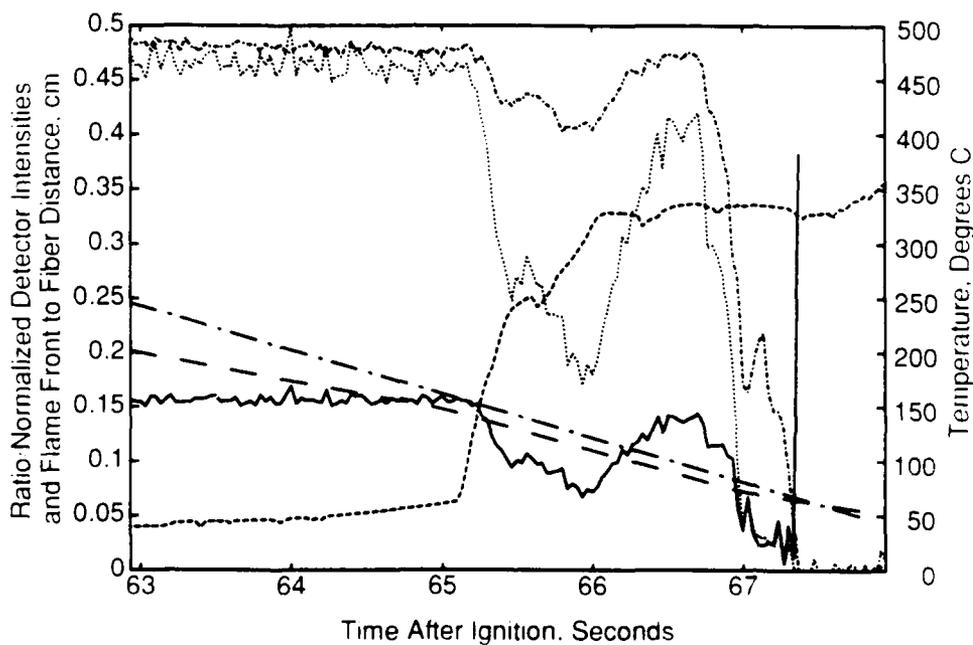


Figure 8. XM39 Burning at 6 atm Pressure. Showing Slow Appearance and Disappearance of N₂O. (Same key as Figure 4.)
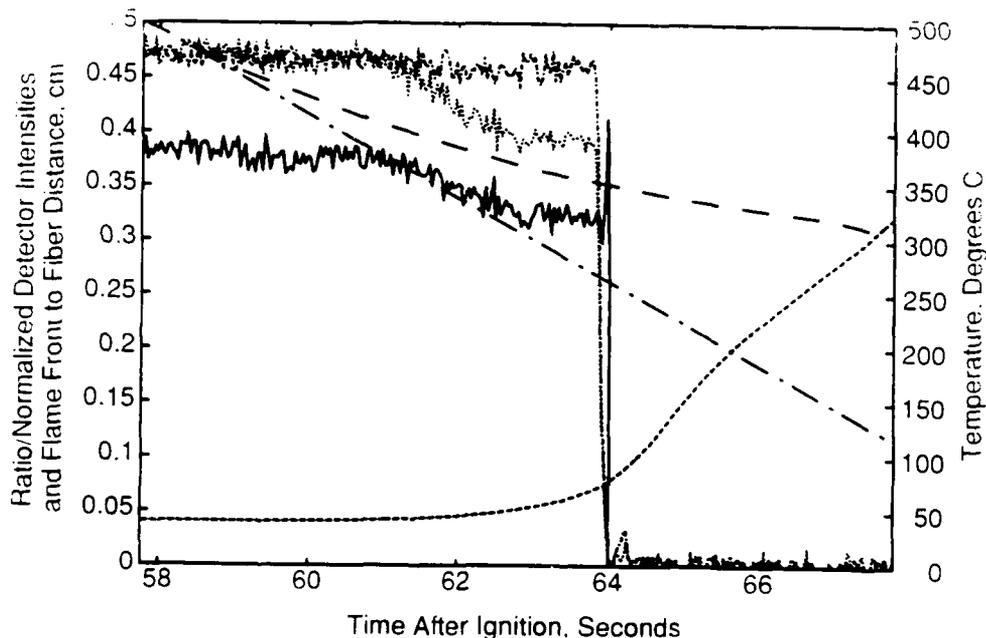
Figure 9. XM39 Burning at 6 atm Pressure, With Kapton Film Inserted Above Fiber Gap.

closer to the flame front through suddenly opening cracks. In two cases, experiments were set up exactly like the series of 6 atm experiments which yielded sudden $N_2O$ appearance, except that before the two segments of propellant strand were joined, a 0.0025 cm thick sheet of Kapton (a strong, high-temperature plastic) was placed on top of the fibers (covering about the central half of the strand surface). With this more solid "roof", no abrupt appearance of $N_2O$ was observed. Instead, the $N_2O$ effused slowly around the plastic sheet and into the observation volume.

### 4.2 Numerical Results

Table 2 lists averages or ranges of some of the parameters which can be derived from the data traces exemplified by Figures 4 through 8. Beginning with the burn rates derived from the video records, it goes on to address five time points in the history of a burn: the appearance of $N_2O$ in the observation region, then two points at which the temperature history changes its functional form, the point at which transmission goes to zero, and finally a point representative of conditions near the flame front. The point-by-point flame front position histories were used to produce distances between the flame front and the fiber at the time when the fiber plane temperature is going through these points. Each of the points requires a few words of definition.

The definition of the $N_2O$ appearance point is straightforward for abrupt cases — for slower filling cases we chose the point at which the ratio drops one standard deviation below its mean for the previous 10 seconds. A criterion based on fitted curves could also be used, but those

Table 2. Averages and Ranges of Quantities Measured in XM39 Experiments

|  | 1 atm (7 cases) | 6 atm (6 cases) |
|---|---|---|
| Burning Rate, cm/s | 0.0150±0.0014 | 0.0410±0.0025 |

$N_2O$ Appearance

| | | |
|---|---|---|
| $N_2O$ Mole Fraction, Range | (0.05-0.19) | (0.05-0.24) |

| Flame-to-Fiber Distance at $N_2O$ Appearance Point, cm | | |
|---|---|---|
| From Point-by-Point Measurements | 0.21±0.11 | 0.16±0.12 |
| From Linear Fit to Flame Front Position | 0.26±0.11 | 0.15±0.11 |

| | | |
|---|---|---|
| Thermocouple Readings at $N_2O$ Appearance, Range, °C | (240-410) | (35-155) |
| Fill Time (from First $N_2O$ to Steady Value), Range, s | (0.3-2.0) [5] | (0.1-0.3) [5] |
| (Numbers of Observations in Brackets) | (0.1-0.2) [2] | (0.7) [1] |
| Steady State Time (for Short Fill Time Cases, Time During Which a Roughly Constant Transmission Indicating $N_2O$ Presence is Maintained), Range, s | (1-2) | (0.3-0.7) |
| $\Delta t_{ff}$, Flame-to-Fiber Distance/Burning Rate, s | (8-28) | (1.7-4.8) |

Change in $\alpha$ Point in Temperature History

| | | |
|---|---|---|
| Distance to Flame Front at $\alpha$ Change Point, cm | 0.34±0.17 | 0.07±0.07 |
| Temperature at $\alpha$ Change Point, °C | 140±30 | 110±40 |

Temperature History Inflection Point

| | | |
|---|---|---|
| Distance to Flame Front at Inflection Point, cm | 0.26±0.085 | 0.05±0.06 |
| Temperature at Temperature History Inflection Point, °C | 200±20 | 185±45 |
| Slope at Temperature Inflection Point, °C/s | 35±15 | 400±200 |

Transmission Loss Point

| | | |
|---|---|---|
| Flame-to-Fiber Distance at Transmission Loss, cm | 0.19±0.07 | 0.08±0.08 |
| Temperature at Transmission Loss Point, °C | (250-500) | (50-330) |

Expected Time of Arrival of Flame Front at Fiber Plane

| | | |
|---|---|---|
| Distance to Flame Front at $\Delta t_{ff}$ after $N_2O$ Appears, cm | 0.06±0.03 | -0.02±0.06 |
| Temperatures at $\Delta t_{ff}$ after $N_2O$ Appearance, °C | 380±45 | 410±90 |
| Slope of Temperature History at $\Delta t_{ff}$ after $N_2O$, °C/s | 10±6 | 100±40 |

points differed by less than 1 second from those derived as above. As will be discussed below, the rise of temperature with time has an exponential form until, at an upper limit temperature, it departs from that dependence. We define that point as the temperature history inflection point, and defer a discussion of its significance to the following section, but for now we can note that even with the often uneven burning in the fiber region, the average values of temperature and temperature rate of change at this point have fairly small uncertainties. Furthermore, in the exponential range of the temperature history, a discontinuous change in the parameters of the exponential is observed. As will be discussed below, this is most easiliy ascribed to a physical change in the propellant which affects the thermal diffusivity (denoted by the symbol $\alpha$), so Table 2 refers to the $\alpha$ change point, although a more neutral term such as gradient change point might be preferred. The transmission loss point is easily defined as the point where one detector intensity came so close to zero that the ratio falls well outside of its previous range of variation.

The most straightforward way to derive a time for the last, flame front arrival event would be to use the time at which the video flame front position history says the flame front is at the fiber plane. However, we have already mentioned that these generally quite smooth variations of flame front positions with time become more irregular near the fiber plane. It turned out that evaluating average quantities at the zero flame-to-fiber distance time led to very wide ranges of variation. If we assumed that the regression of the center of the strand was more regular, we could instead use the linear fits to derive a time for flame front arrival. In Table 2 we use a third method, extrapolating from a point where we expect the flame front and burning rate to be relatively unperturbed. This point could be defined in a variety of ways, but we chose it to be the $N_2O$ appearance point, simply because its flame-to-fiber distance was of intrinsic interest and already had been tabulated. This distance and the burning rate are used to derive a time between $N_2O$ appearance and the arrival of the flame front, $\Delta t_{ff}$, reported in the $N_2O$ appearance section. This time is then added to the $N_2O$ appearance time to generate a time at which to evaluate properties which may represent conditions near the flame front. Simply as a check, we evaluate the position relative to the flame front from the video record for these times. As can be seen in Table 2, on the average the video flame front is very close to the fiber plane at $\Delta t_{ff}$ from $N_2O$ appearance for the 6 atm cases, but appears to be slightly above the fiber plane in the 1 atm cases.

It is of interest to examine the flame-to-fiber distance entries in Table 2 to establish the sequence of events experienced at the fiber insertion plane. The sequence is different at the two pressures. At 1 atm, the temperature inflection point can arrive first, followed in fairly rapid succession by the appearance of $N_2O$ and the loss of transmission, with the arrival of the flame front occurring considerably later. At 6 atm, the $N_2O$ appears first, substantially before the arrival

16

of the temperature inflection point, and therefore in a lower temperature regime. Loss of transmission, inflection point arrival, and arrival of the flame front region as defined by the above procedure, all occur at about the same time. In the following section, we will show that these changes in the sequence of events follow naturally from the dependence of the thermal wave on the burning rate and the assumption that the length that $N_2O$ can travel through the propellant is less dependent on the burning rate and more a constant of the material.

# 5.0 THERMAL WAVE ANALYSIS

Before we can hypothesize about the source of the $N_2O$ we observe, we must understand why it appears in two different temperature ranges for the two pressure regimes. We can analyze the thermocouple temperature records using a model which utilizes information on the thermophysical properties of the propellant. This is of interest not because it provides accurate measurements of these properties (again, individual burns showed wide variations in almost all observed parameters), but because it will be found that the thermophysical properties derived from the average parameters for all burns are roughly consistent with literature values, and so the expected time/temperature history based on those known thermophysical parameters can be used to interpret our results.

It has long been known[13] that solution of the heat balance equation for a thermal wave with a constant surface temperature progressing into a solid having constant thermal properties and no heat sources or sinks leads to an expression for the steady state temperature profile which has the generalized form,

$$(T-T_0) = (T_{infl}-T_0)exp(-(x-X_0)/\delta). \tag{1}$$

In this expression, x is the (positive) distance into the propellant from the flame front, T is the temperature at x, and $T_0$ is the ambient temperature. From the derivation, $T_{infl}$ is the temperature at which the thermal wave departs from exponential behavior, which occurs at the plane where heat production ( ) becomes important. The effect of this heat source is seen in the shallower temperature gradient in the non-exponential region, a gradient extending further into the solid due to heat production. In the early work on double-base propellants, $T_{infl}$ could be identified with the burning surface temperature $T_s$. It will be seen that this is not the case for the composite propellant studied here, since Table 2 shows that a departure from exponential behavior occurs at a much lower temperature than the surface temperature. This difference results in a second modification to the exponential expression, the presence of the parameter $X_0$ which is the distance between the flame front and the temperature history inflection point. Finally, the length scale parameter $\delta$ is related to the thermal diffusivity $\alpha$ and the burning rate $r_b$ by

$$\delta = \alpha/r_b \tag{2}$$

Equation 2 represents a competition between the ability of heat to move through the solid and the speed of the flame consuming the solid. If the former is large, $\delta$ is large and heat penetrates a long

18

distance into the solid. When the burning rate is relatively large, $\delta$ is small and the temperature gradient extends only a short distance into the propellant. The thermal diffusivity is in turn related to the thermal conductivity $\lambda$ and the heat capacity $c_p$ by $\alpha = \lambda/\rho c_p$ where $\rho$ is the density. Our observations, of course, do not shed any light on these quantities individually.

The applicability of a simple model becomes clearer when the temperature with time data are displayed in a semilog plot, as in Figures 10 and 11. It is seen that simple exponential forms fit very well over two temperature regions. The parameter $\delta$ is derived from such plots by dividing the average burn rate by the slope of each temperature versus time curve. Therefore, to begin by representing the temperature histories in the smallest number of parameters, we fit two exponential length scale parameters, $\delta$, to each case, then computed a mean and a standard deviation for each pressure and temperature regime. These parameters are reported in Table 3. Then we used the inflection point temperatures and positions reported in Table 2 to solve for a pre-exponential factor $C$, in

$$(T - T_0) = C\exp(-x/\delta) \tag{3}$$

These parameters are also reported in Table 3.

A point which should be mentioned now is that the assumption that the change in gradient parameters between the two temperature regions corresponds to a discontinuous change in the thermal diffusivity (perhaps due simply to bubbles or cracks appearing at the transistion temperature) is only one possible explanation. Another is that the steep exponential region between the two transition temperatures is due to an endothermic process such as melting or boiling. The drawback to this alternative is that the exponential form would not be expected to hold, without a fortuitous dependence of the rate of heat loss on temperature.

If we keep the hypothesis that the transition between two exponential gradients involves a change in thermal diffusivity, we must next address the fact known from other work that the thermal diffusivity is a function of temperature. Experiments in the -20 to 50 °C range have yielded a three parameter fit to $\alpha(T)$[14]. Having shown that we can represent our observed data in terms of simple exponential forms, we now want to show that those data are consistent with a plausible temperature dependent thermal diffusivity. For a temperature dependent $\alpha$, the closed form Equation 1 does not obtain. However, it will be sufficient to approximate the true (non-closed-form) solution by Equation 1 with a temperature dependent $\alpha$, and to use a linearly temperature dependent $\alpha(T)$, $\alpha(T) = \alpha_0 + \alpha_1 T$, because all we want to do is show that our data are
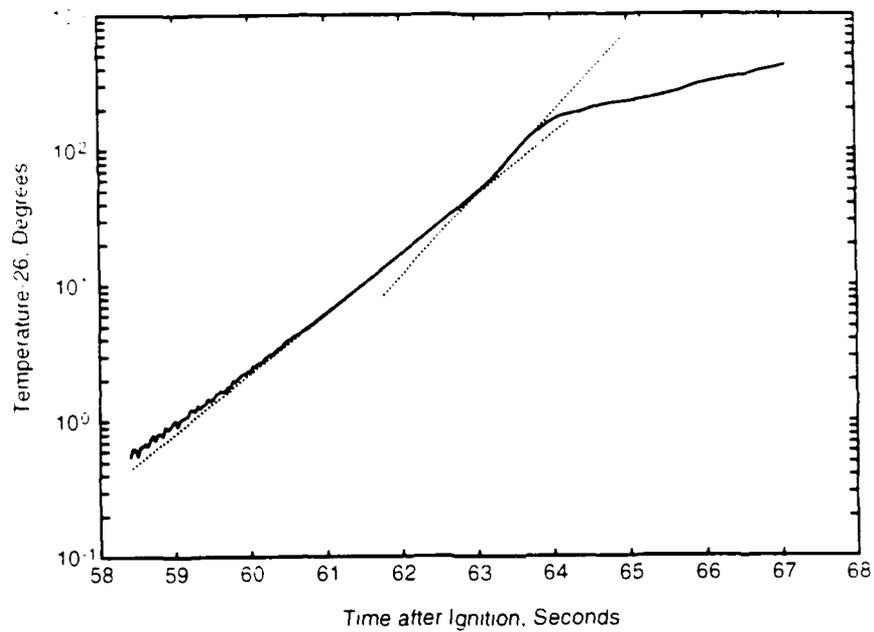
Figure 10. Temperature History of 6 atm Case Shown in Figure 4, Showing Fits to Simple Exponential Expressions (Dotted Lines).
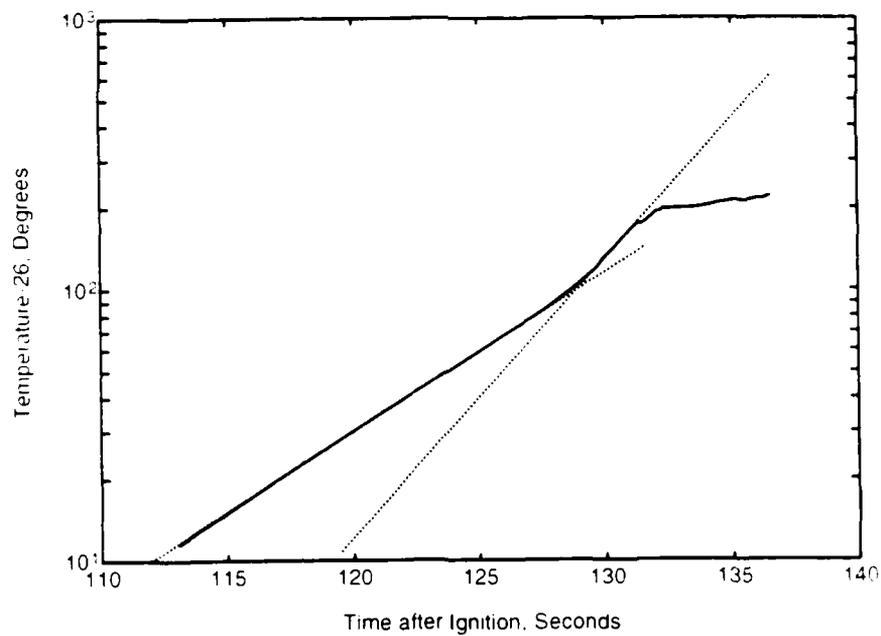


Figure 11. Temperature History of 1 atm Case Shown in Figure 5, Showing Fits to Simple Exponential Expressions (Dotted Lines).

Table 3. Parameters Obtained from Thermocouple Temperature Histories

| Exponential Fit to Low Temperature Range | 1 atm | 6 atm |
|---|---|---|
| $\delta$, Length Scale Parameter, cm | 0.165±0.032 | 0.042±0.0065 |
| C, Pre-exponential Factor (Uncertainty Range),°C | 595 (430-620) | 330 (185-430) |
| **Exponential Fit to High Temperature Range** | | |
| $\delta$, Length Scale Parameter, cm | 0.095±0.044 | 0.024±0.009 |
| C, Pre-exponential Factor (Uncertainty Range), °C | 2680 (1260-25200) | 1090 (825-2470) |
| **Model Parameters Consistent with Exponential Fit** | | |
| $T_{infl}$-$T_0$, °C | 174 | 160 |
| Thermal Wave Origin, $X_0$, cm | 0.26 | 0.045 |
| **Low Temperature Range** | | |
| Thermal Diffusivity Constant Term, $\alpha_0$, cm$^2$/s | 0.0019 | |
| $\alpha$ Temperature Coefficient, $\alpha_1$, cm$^2$/s °C$^{-1}$ | $9 \times 10^{-6}$ | |
| **High Temperature Range** | | |
| Thermal Diffusivity Constant Term, $\alpha_0$, cm$^2$/s | 0.0014 | |
| $\alpha$ Temperature Coefficient, $\alpha_1$, cm$^2$/s °C$^{-1}$ | $2 \times 10^{-6}$ | |

noisy enough that it is difficult to distinguish between a constant and a temperature-dependent thermal diffusivity.

To do this, we use the Equation 3 representations of average temperature histories, together with upper and lower error limit expressions derived as follows. The $\delta$ parameter in the upper limit expression is the average $\delta$ plus its standard deviation. The C parameter for the high temperature range is then obtained by fitting to the inflection point temperature plus its standard deviation. The C parameter for the low temperature range is set by matching the high temperature expression at the $\alpha$ change point. Since the $\delta$ parameters, which appear in the exponential, have fairly large standard deviations, and since the range of observed temperatures at any distance from the flame front is relatively small, the C parameters are forced into some large variations, as seen in the ranges reported in Table 3.

To show how these exponential forms compare with some individual observations, Figures 12 and 13 once again exhibit the temperature data for the two cases shown in Figures 10 and 11. Here, however, the video flame front position record has been used to convert the time axis into a distance from flame front axis. The exponential data representations using the parameters in Table 3, and the uncertainty limit expressions derived as discussed above, are also plotted in the figures. It can be seen that the substantial *variations in the* distance scales cause these observed curves to fall outside the error limit expressions. In the 6 atm case, the observed inflection and $\alpha$ change points occur at 0.10 and 0.13 cm from the flame front, much further out than the average values of 0.05 and 0.07 cm. In the 1 atm case, on the other hand, inflection and $\alpha$ change point at 0.22 and 0.26 cm are well inside the average values of 0.26 and 0.34 cm. However, the uncertainty in the position axis does not directly affect the determination of thermal diffusivity values from the slope of the temperature history curve.

Now that we have a compact way of expressing what, on average, the temperature histories were in the two pressure regimes, we can go on to compare to expected temperature histories as predicted by Equation 1. In Figures 14 and 15 we present the Equation 3 exponential data representations as dashed lines, with the error limits expressions again yielding two bracketing dotted lines. The solid lines are given by Equation 1 using the parameters in the lower half of Table 3. The pre-exponential factor C can be divided into the inflection point temperatures given in Table 2 and exponentials involving $X_0$ parameters which are essentially the average observed positions of those inflection points. The linear $\alpha(T)$ expressions given by the parameters in Table 3 are those which minimize the squared differences between the dashed and solid lines in Figures 14 and 15. These linear thermal diffusivity expressions are plotted in Figure 16, along

22
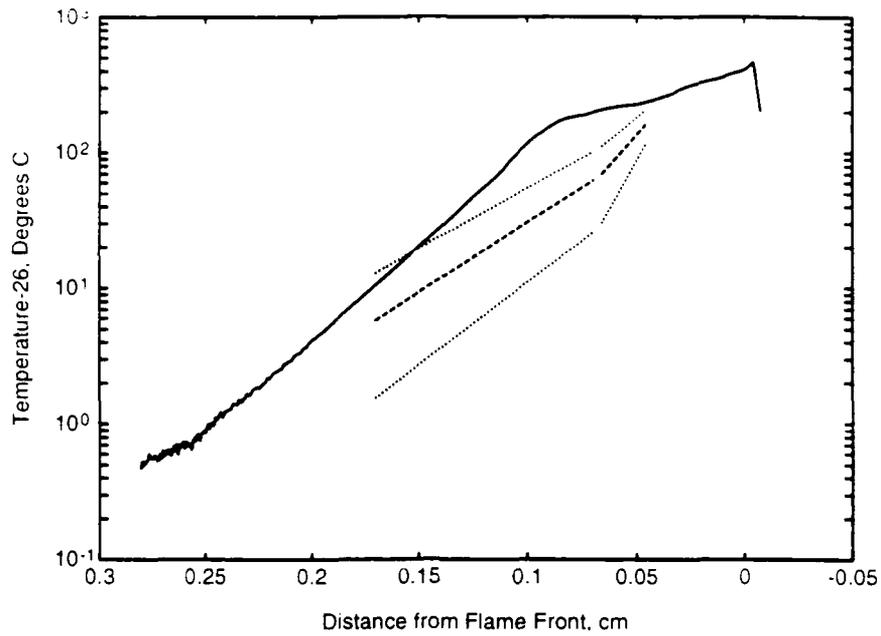
Figure 12. Thermocouple Reading versus Flame Front Position of 6 atm Case Shown in Figure 4 (Solid Line), Average Exponential Data Representations (Dashed Lines), and Error Limit Expressions (Dotted Lines).
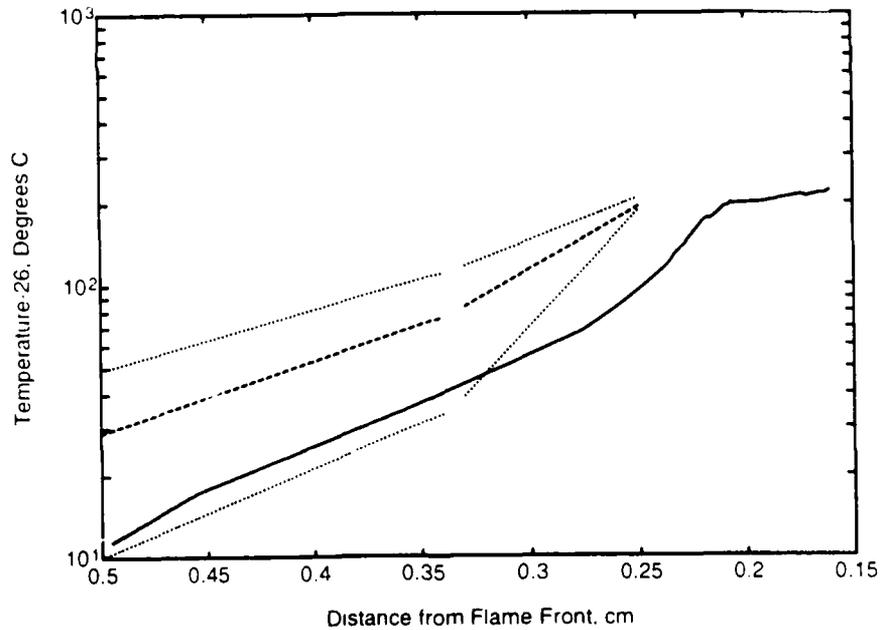


Figure 13. Thermocouple Reading versus Flame Front Position of 1 atm Case Shown in Figure 5. (Line types have same definitions as in Figure 13.)

23
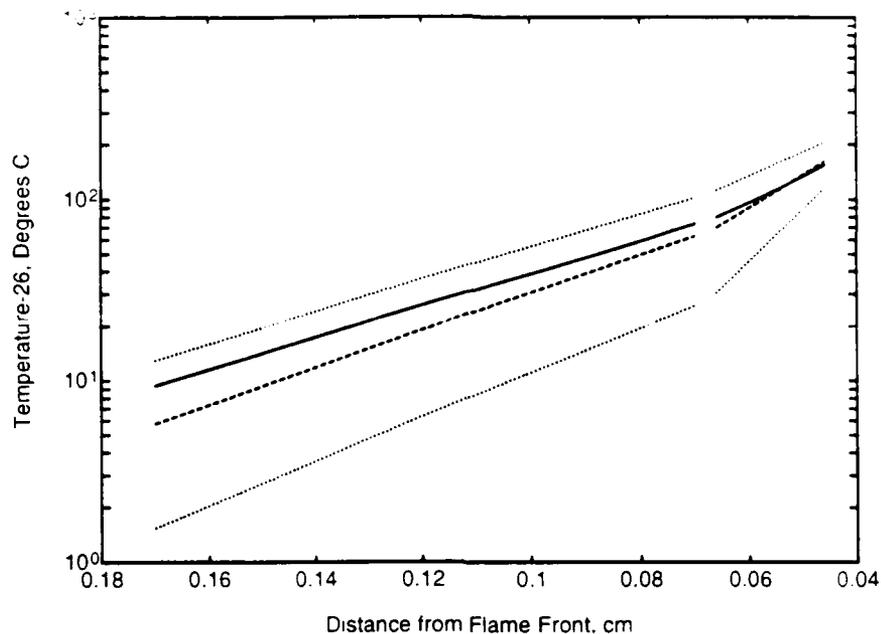
Figure 14. Comparing Simple Exponential Data Representation and Error Limit Expressions for 6 atm Cases (Dashed and Dotted Lines) with Equation 1 Expression Including Temperature-Dependent Thermal Diffusivity and Other Table 3 Parameters (Solid Lines).
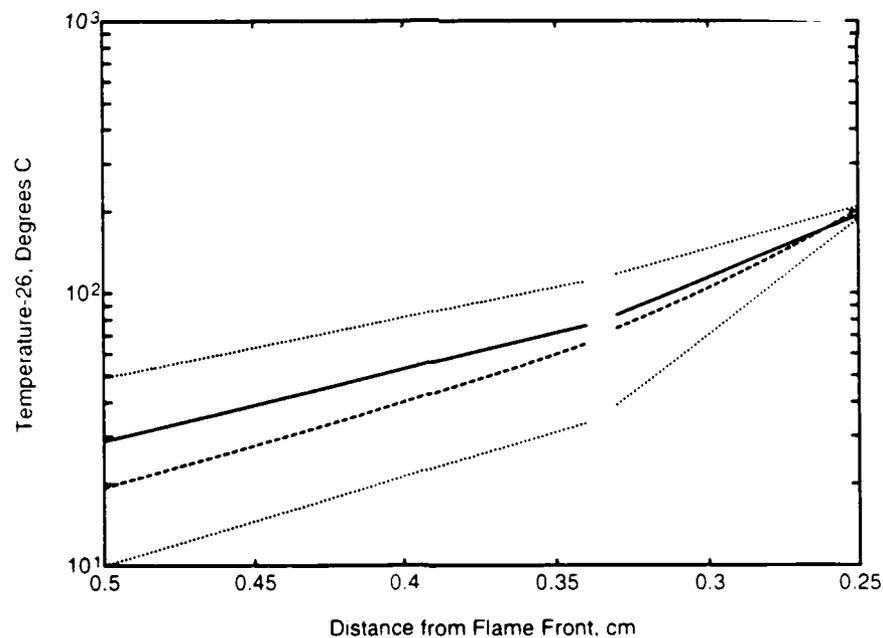


Figure 15. Comparing Simple Exponential Data Representation and Error Limit Expressions for 1 atm Cases (Dashed and Dotted Lines) with Equation 1 Expression Including Temperature-Dependent Thermal Diffusivity and Other Table 3 Parameters (Solid Lines).

24

Figure 16. Thermal Diffusivity for XM39: Low Temperature Measurements[14] (Solid Line), Data Point from Strand Burning Observations of Reference 15 (With Quoted Error Limits, Plotted at Observed Inflection Point Temperature of 165 °C), and Our Linear α(T) Expressions From Table 3, Used in Figures 14 and 15. (Dot-Dash and Dashed Lines).

parameters which give the best match between Equation 1 and Equation 3 expressions while still being roughly compatible with the other measurements of α,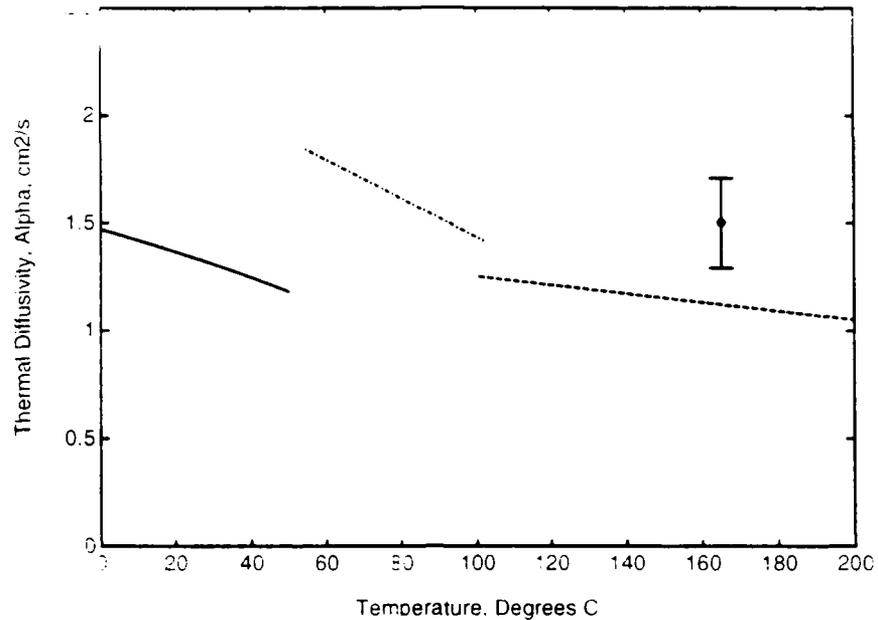 many other α(T) values would also fit our observations well enough. This is shown in Figure 17, which shows a region of α(T) values which give temperature history curves which lie within the error limit expressions for *both* the 1 atm and 6 atm cases. In other words, the uncertainty in what values of α(T) are consistent with our observations is at least as large as indicated in Figure 17. Considering these large uncertainties, it is not a matter of great concern that our average α values at low temperatures seem to be higher than those of Reference 9, nor that our high temperature α values seem to be below that reported in Reference 15.

To summarize, a single set of α(T) expressions can be used to reproduce the average temperature histories for both the 1 atm and 6 atm data sets. This is in spite of the fact that (at the simple exponential level of data analysis) the average δ parameters for the two data sets are not in the ratio of the burning rates for the two pressures ($r_b$(6 atm)/$r_b$(1 atm) = 2.7 ± 0.3), but instead, the ratios in both temperature regimes are about 4. However, the uncertainties in the ratios of δ(6 atm) to δ(1 atm) are large (±1.0 and 2.4 for low and high temperature ranges), so much of the difference can be put down to large standard deviations, with a component also potentially ascribable to the temperature dependence of α and the fact that somewhat different ranges of temperature contribute to single values of α derived from the two different pressure cases.

25

To summarize, a single set of $\alpha(T)$ expressions can be used to reproduce the average temperature histories for both the 1 atm and 6 atm data sets. This is in spite of the fact that (at the simple exponential level of data analysis) the average $\delta$ parameters for the two data sets are not in the ratio of the burning rates for the two pressures ($r_b(6\ atm)/r_b(1\ atm) = 2.7 \pm 0.3$), but instead, the ratios in both temperature regimes are about 4. However, the uncertainties in the ratios of $\delta(6\ atm)$ to $\delta(1\ atm)$ are large ($\pm 1.0$ and 2.4 for low and high temperature ranges), so much of the difference can be put down to large standard deviations, with a component also potentially ascribable to the temperature dependence of $\alpha$ and the fact that somewhat different ranges of temperature contribute to single values of $\alpha$ derived from the two different pressure cases.
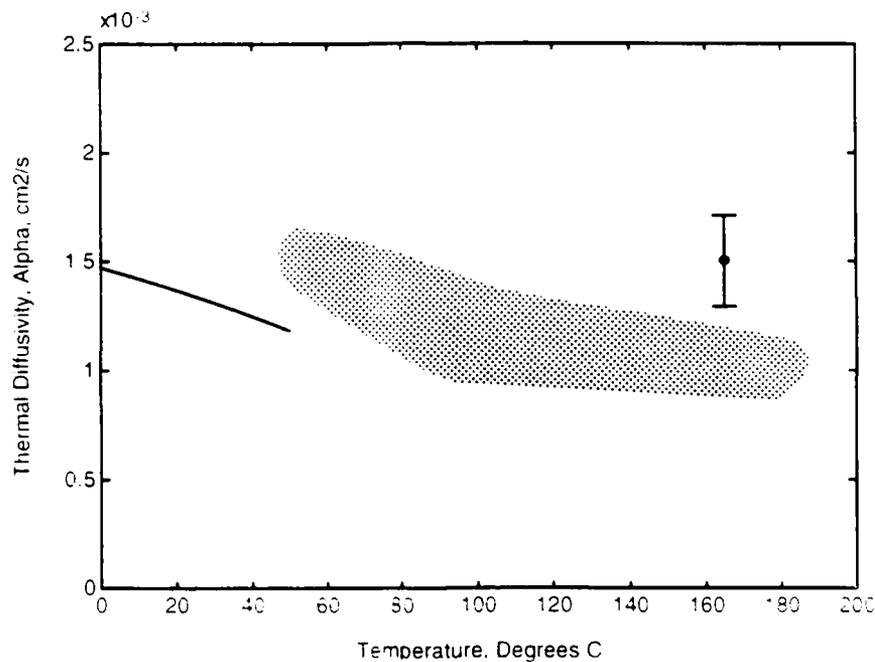


Figure 17. Thermal Diffusivity for XM39: Low Temperature Measurements[14] (Solid Line), Data Point from Strand Burning Observations[15], and Range of Values whose Equation 1 Temperature Histories Fall within the Error Limit Regions in Figures 14 and 15 (Dots).

# 6.0 DISCUSSION

This study has produced three major results. The first is that we have observed $N_2O$, a gaseous decomposition product of RDX, evolving into a small volume in the condensed phase of a burning nitramine propellant strand. As we will discuss below, this result is expected, in that it is consistent with other observations of the chemistry of RDX decomposition. The second is that in the 1 atm cases, there is strong evidence that $N_2O$ is not seen until substantially after the RDX melting and decomposition processes have begun. It has been expected that $N_2O$ is not a primary product of RDX decomposition, but it is somewhat surprising to see such a clear separation. The third result is that many 6 atm cases show an abrupt $N_2O$ evolution at a time when the propellant forming the observation volume is still at a temperature well below that needed to produce rapid decomposition of RDX. We can suggest a mechanism for this observation, but first we need to place it in the context of what we and others have learned about XM39 burning and RDX decomposition.

## 6.1 Correlation of Observed Events with Temperature History

To aid in visualizing the relationships between the events listed in Table 2, in Figure 18 we present a sketch of temperature histories and event positions and temperatures which are roughly consistent with those in the table. It turns out that it is not possible to construct a self-consistent graph out of the averages listed in Table 2, because the large variances and small numbers of points mean that different runs have different weights in determining the various parameters. Even such basic qualitative characteristics as the order of events cannot be completely summarized by a single figure. For example, although four 6 atm runs do indeed have the order shown in the figure, $N_2O$ appearance/transmission loss/$\alpha$ change/inflection point, two others have a different order, $\alpha$ change/$N_2O$ appearance/inflection point/transmission loss. Still, to the extent that there is a typical set of positions and temperatures associated with the set of observed events, Figure 18 is as good a representation of it as our present data set will allow.

In the context of Figure 18, then, we want to ask what we know about the state of the propellant through the time interval surrounding the observation of $N_2O$ appearance in the observation region, based both on our data and on other sources. We begin by noting that in Table 2, three of the events are associated with temperatures with fairly small standard deviations, suggesting that they involve processes which are legitimately associated with specific temperatures. The burning surface, of course, is expected to have a temperature which is only secondarily a

27
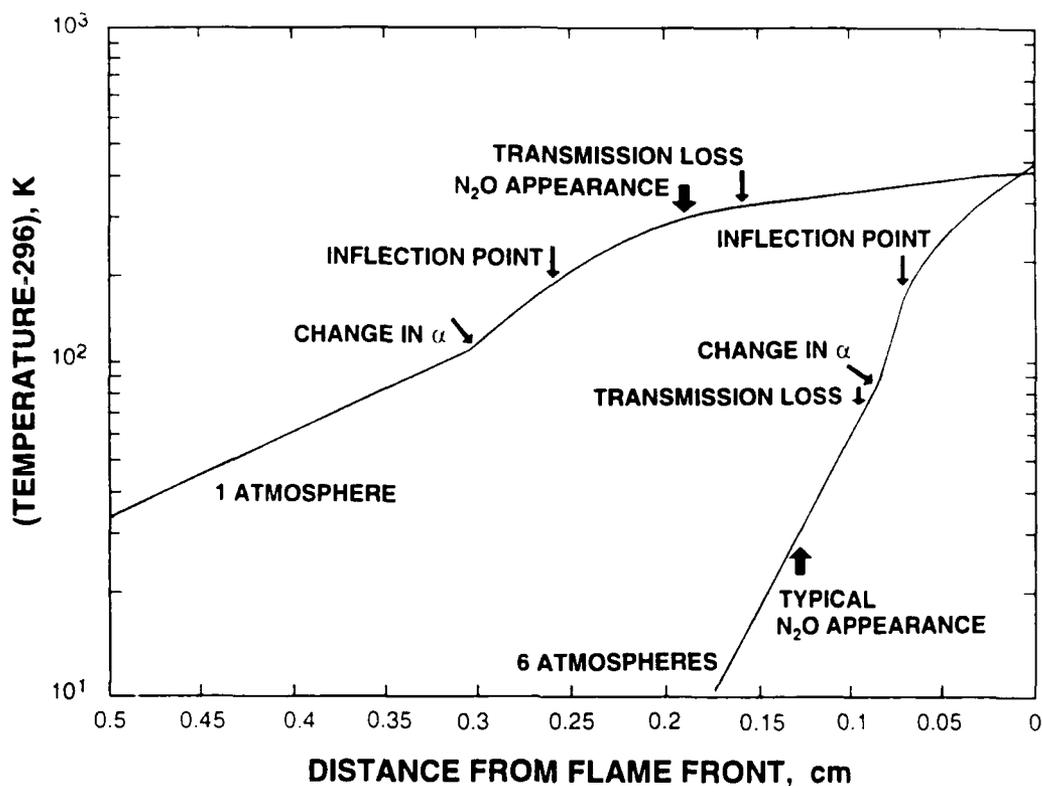
Figure 18.    Qualitative Sketch of Typical Thermal Waves and Positions of Other Events in Strand Burning Observations

function of combustion pressure (although our strand burning in air is certainly expected to have a higher surface temperature than observed in inert atmospheres). The value from our extrapolation procedure for the time of arrival of the flame front, of about 400 °C, is consistent with the range quoted by Brill and Brush[16] of 350-400 °C for the surface temperature of burning HMX and RDX.

Again, the temperature inflection point, occurring around 190 °C, is thus not to be identified with the burning surface temperature. This conclusion is reinforced by the fact that in 1 atm cases we have good infrared transmission over a long path through a channel in the solid long after the inflection point has passed the observation region. We know the major component, RDX, does not decompose at significant rates until it has melted. Consulting Table 1, we find that RDX melts at 190 °C. (This value is a manufacturer's specification—the references to values in the 203-205°C range may refer to material of higher purity than would be found in gun propellant[2,6,17].) Therefore, our inflection point may be associated with the melting, decomposition, and eventual heat releasing processes in RDX. It is clear that if RDX melting begins at the inflection point temperature, its effect on the temperature history is masked by the exothermic process. An

alternative explanation, that what we have referred to as the α change point is actually the RDX melting point, would shift all our observed temperatures to surprisingly high values.

Because these processes take place at finite rates, as the burning rate increases we expect the inflection point to shift to higher temperatures, as seen in the observations of Reference 15. These covered the pressure range from 75 to 750 psig, and showed a strong dependence of the inflection point on pressure  The temperatures reported at the two extreme pressures are about 165 and 370 °C, respectively, while at 200 and 500 psig the temperatures are 250 and 300 °C.  It can be seen that the expected variation from 1 to 6 atm is smaller than our standard deviations, so our failure to observe this trend is not surprising.

Finally, we want to ask if the lower temperature change in the form of the thermal wave, which we have referred to as the α change point, can be identified with a property of one of the propellant ingredients.  If we note the temperature ranges in Table 2, centered around 125 °C, and then consult Table 1, we find the closest temperature listed to be the boiling point of the plasticizer. Acetyl triethyl citrate is a liquid at room temperature, and its plasticizing action essentially involves partial solvation of the other propellant ingredients.  The thermal properties of this solution will be different than those of the pure liquid plasticizer, but it is not unreasonable to expect a sharp change in properties near the plasticizer boiling point, due to either vaporization or thermal decomposition. Here again it must be remarked that in their observations of strand burning of XM39 with embedded thermocouples, neither Reference 9 or 15 noted such a point in the temperature history. We can only suggest that at their higher pressures and faster time scales, the process involved is too slow to be observed as a sharp discontinuity.  This point too is not seen by us to move towards higher temperatures at faster burning rates, but again our error limits are substantial.  We should also note again that the steeper gradient between inflection and α change points may not be a thermal diffusivity effect at all, but simply reflect a heat consumption process such as melting, boiling, or thermal decomposition.

Having made the case that three of the events identified in Table 2 and Figure 18 are, under our conditions, correlated with relatively fixed temperatures, what can be said of the other two events?  It is clear that transmission loss is not correlated with temperature, and the wide variation in temperatures at which it occurs tells us that a number of different processes can be involved in bringing the transmission to zero, including misalignment of the fibers and intrusion of molten propellant material into the observation region.  It turns out, however, to be fairly well correlated with distance from the flame front, with the standard deviation in position for the 1 atm cases being particularly small.

Finally, it is clear from Figure 18 that appearance of N$_2$O in the observation volume is not correlated with the temperature at that point. If anything, it too is better correlated with distance from the flame front. To understand why we suggest that the N$_2$O we observe has been formed not in the observation region, but substantially nearer the flame front, we need to review what we know about combustion of nitramine propellants like XM39.

First, we know that N$_2$O is a product of thermal decomposition of RDX, but not a final product of the gas phase combustion of those solid decomposition products, either in the primary flame or in secondary combustion with added oxygen. The evolution of N$_2$O from heated RDX has been observed by a number of investigators, using mass spectrometric and infrared absorption detection techniques.[3,6,11,16,18] An example of the quantitative measurements of Fetherolf and Litzinger[11] is given in Figure 19, along with our estimate of how the somewhat broader range of species observed by Behrens[18] in his low pressure experiments would evolve under the 1 atm conditions of Reference 11. The point of this figure is that under a wide range of conditions N$_2$O is expected to be a major gas phase product of the thermal decomposition of RDX. The second point, that N$_2$O is not expected to be a major product of gas phase combustion of RDX decomposition products, is made by Figure 20. It shows results of the gas phase chemistry calculations of Melius[19,20] for RDX burning in 1 atmosphere of an inert gas. In his mechanism, N$_2$O is consumed by thermal decomposition as well as reaction with hydrogen atoms, and has essentially disappeared 0.1 cm above the burning surface. Thus, we know that the gas we are observing comes from inside the condensed phase of the propellant, not from the exhaust gas from the flame. In any case, the rapid gas flow over the strand prevents recirculation of the exhaust gas into the fiber insertion region.

We also know that measurements of the kinetics of RDX decomposition show that gas evolution is very slow below the melting point.[5,18,21] Yet we also know that infrared transmission through even 0.1 cm of molten propellant will be essentially zero, so that the walls of the observation region must be, at least, below the melting point of the CAB binder (215-225 °C). Further, we know that the N$_2$O appearance rate in cases like those of Figures 4 and 5 is faster, by one to two orders of magnitude, than could be expected from N$_2$O evolution from the walls of the observation region, when the observed evolution rate from Reference 18 for RDX at 205 °C is used. All these facts lead us to suggest that N$_2$O from RDX decomposition accumulates in pressurized bubbles in regions of the propellant strand which are hotter and closer to the flame front than the observation region, and that the N$_2$O is transported from the pressurized bubbles to the observation volume by the opening of cracks connecting the two regions.
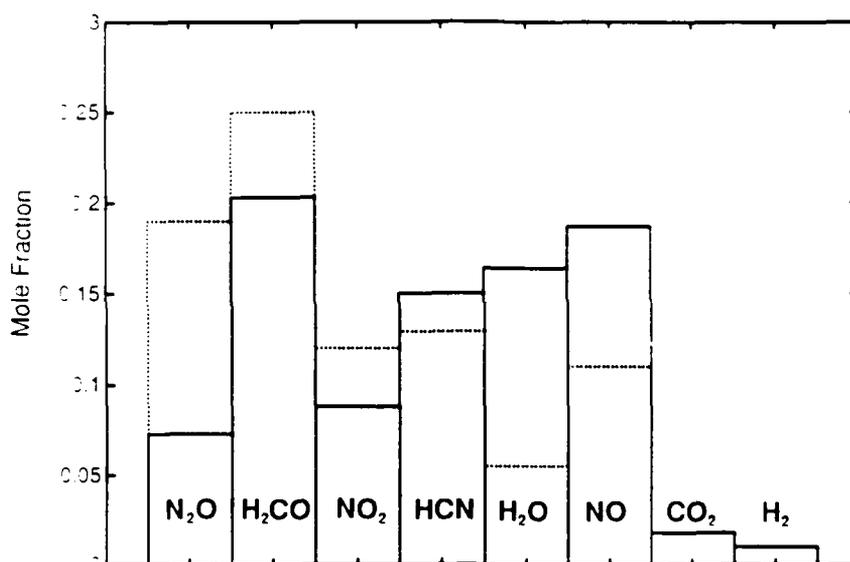
Figure 19. Major RDX Decomposition Gas Species from Experiments of Fetherolf and Litzinger.[11] Compared to Adaptation of Observations of Behrens (dots)[18]
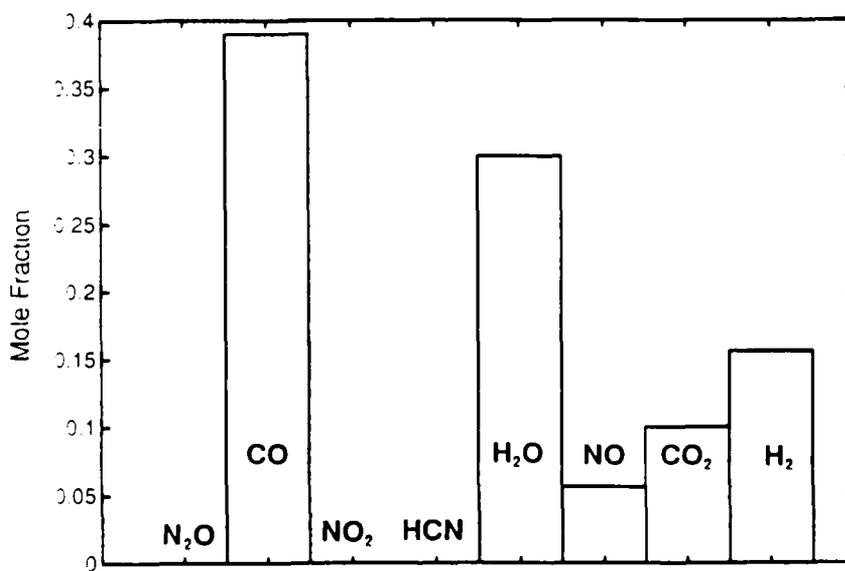


Figure 20. Major Gas Phase Products of RDX Primary Combustion, from Model Calculations of Melius.[19,20]

Several groups have made scanning electron microscope (SEM) observations of sections through the surface of quenched strands of XM39.[15-22] A melt region is observed, of thickness 0.01-0.03 cm for burning in air at 1 atmosphere pressure. This melt region is filled with bubbles of various sizes, ranging in diameter up to the full thickness of the melt layer. Because these bubbles are so close to the burning surface, it would be surprising if they were the source of $N_2O$ observed on the order of 0.1 cm further down, in relatively still-solid propellant. We would expect most of these bubbles to burst upward, ejecting decomposition gas into the flame, and indeed what we could see of our burning surfaces seemed to be consistent with a melt layer containing growing and bursting bubbles. Furthermore, a single bubble, even with a 0.03 cm (300 μm) diameter, will not fill the observation region, a cylinder of 0.02 cm diameter and order of 0.3 cm length, to the mole fraction levels we observe, which are consistent with pure decomposition gas at ambient (1 or 6 atm) pressure.

These objections lead to the suggestions that the bubbles, or pressurized voids, which are the source of the $N_2O$ we observe, are not in the melt region but below it, in a region where at least the higher-melting binder has kept enough strength to hold these bubbles in place, and that our observations of sudden filling of the observation volume with $N_2O$ involves the nearly simultaneous opening of several cracks connecting it to several bubbles. Such cracks have not, to our knowledge, been observed in any SEM photographs of XM39 strands, but there need not be many of them, and they will be more difficult to see than the bubbles. Finally, we cannot at this point rule out the possibility than our fiber insertion procedure, involving pressing a groove at least 0.01 cm deep into the propellant, has generated fractures extending many times that depth into the solid, or has at least set up strains which make crack formation more likely during burning.

6.2 Correlation of Our $N_2O$ Observations with Chemical Mechanisms of RDX Decomposition

This last part of our discussion has to do with the status of $N_2O$ as a major decomposition product of RDX. It turns out that the observation of substantial $N_2O$ is completely consistent with the existing literature of experiments, theoretical predictions, and analysis. To show this, we present a brief review of some of the major contributions to the current overall picture of RDX decomposition.

It has been widely noted[16, 18, 20] that there appear to be two global decomposition channels for RDX, one leading to the products $N_2O + H_2CO$, and one leading to $NO_2 + H_2CN$ (or $HONO + HCN$, or $NO_2 + HCN + H$, the differences expressing the fact that some of the products of this channel are less stable). The pathways to these products can include a number of parallel

processes, some of which can involve a number of sequential steps. Not surprisingly, then, some variation in relative amounts of the above products and others has been observed depending on the conditions during the decomposition. Experiments on RDX decomposition under relatively controlled conditions, including the use of deuterium isotope techniques, have unraveled some of the details of these processes.

Behrens and Bulusu[18] have been able to explain their simultaneous thermogravimetry modulated beam mass spectrometry observations of RDX thermal decomposition under high vacuum conditions using four pathways:

1. Formation of 1-nitroso-3,5-dinitrohexahydro-s-triazine (ONDNTA — RDX with one $NO_2$ group replaced by NO) followed by ring breaking to yield $N_2O$, $CH_2O$, and other products.

2. HONO elimination to form oxy-s-triazine (OST), a molecule which retains the C-N ring of RDX and has the formula $C_3H_3N_3O$ and an uncertain structure, as well as $H_2O$, NO, and $NO_2$.

3. $N-NO_2$ bond breaking leading to ring breaking and formation of $NO_2$ + $H_2CN$ + $2N_2O$ + $2CH_2O$.

4. Catalytic decomposition to form $N_2O$, $CH_2O$, $NO_2$ and $NH_2CHO$.

They find no evidence that process 4 is the water catalysis suggested by Melius[28], and instead suggest the catalyst is a residue of RDX decomposition which builds up on the walls of their reaction cell. That makes this mechanism specific to their apparatus, although analogous processes might occur in the burning of an RDX composite propellant. The other three mechanisms all involve N-N bond breaking, since process 1 is thought to proceed by $N-NO_2$ bond cleavage followed by reaction with a source of NO.[29] This might seem to be in conflict with the deuterium kinetic isotope effect studies of Shackelford et al.[30,31] who found C-H bond rupture to be the rate-controlling step. However, Melius[28] has pointed out that not only does $N-NO_2$ bond breaking weaken remaining bonds, but C-H bond breaking results in a negative $N-NO_2$ bond energy with only a 2 kcal-mole$^{-1}$ barrier for leaving. Furthermore, Behrens and Bulusu found evidence of C-H bond breaking in both pathways 1 and 2, which together result in two-thirds of the total RDX decomposition in their experiment. Behrens and Bulusu also note that pathway 3, whose contribution is estimated to be only 10% of the total, may be the concerted symmetric triple fission to form three methylenenitramine fragments observed in the gas phase by Zhao et al.[32], or may instead be a process yielding two methylenenitramine molecules plus $H_2CN$ and $NO_2$.

To summarize, the above experimental evidence seems to give a coherent picture which agrees with the prediction of Melius[28] on energetic grounds that RDX decomposition in the condensed phase will be dominated by processes involving $N-NO_2$ bond breaking, at least at high heating rates where catalytic processes are not important. The dependence of processes and product distributions on heating rates is part of a more general dependence on the environment of the RDX molecule, including not only the temperatures and time scales involved but also the phase (process 1 is thought to be dominant in the solid phase, and at low temperatures in general). Table 4 gives a review of experimental observations of RDX decomposition to give $N_2O$ ordered by heating rate. It can be seen that the only experiments in which conditions did not allow progress beyond the initial $NO_2$ loss step are those of Wight and Botcher[25-27] (although with longer laser pulses they could observe formation of other products including $N_2O$). As to the rest of the experiments, covering five orders of magnitude in heating rate, it is not easy to discern any systematic trends in product distributions, given that differences in observed concentrations are only at the factor of two level and that other differences in the experimental conditions can also easily generate differences at the same level. Our experiments (with heating rates taken from the temperature history slopes in Table 2) are seen to be in the middle of this range of heating rates.

We can add the comment that the nature of the initiating process for RDX thermal decomposition has been particularly controversial because of a seeming disagreement between the above-mentioned results of infrared multiphoton dissociation experiments by Zhao et al.[32] showing that two-thirds of their RDX decomposed by a concerted detrimerization process, and the condensed phase experiments which find little or no evidence for such a process. However, the suggestion has been made by Wight and Botcher[27] that in fact no discrepancy exists, that while the concerted process proceeds easily in the vapor phase, the condensed phase constrains the motion of the RDX molecule too much for it to contribute significantly. Thus the picture of RDX decomposition in the condensed phase remains one in which all ring-breaking proceeds by several sequential steps and results from the destabilizing effects of $NO_2$ loss.

Our experimental observations of $N_2O$ are consistent with the above picture. Our heating rates are slow compared to chemical reaction rates, and our $N_2O$ originates in a mixed gas/liquid region with plenty of opportunity for homogeneous or heterogeneous reactions to carry initial products of decomposition to secondary products. A decomposition product whose observation would tell us more about the environment in the decomposition region and during their transport through the propellant is $NO_2$, which is expected to be more reactive as well as being formed by some of the first bond-breaking processes in RDX. Therefore, in ongoing work, we plan to look

for $NO_2$ simultaneously with $N_2O$, with the other experimental parameters remaining much the same.

Table 4. $N_2O$ Formation at Various Heating Rates

| Research Group | Technique | Ref. | Heating Rate, K/s | $N_2O$ Observed |
|---|---|---|---|---|
| Karpowicz and Brill | Rapid-Scan FTIR Spectroscopy | 2 | 2.5 | Yes |
| Oyumi and Brill | In Situ Rapid-Scan FTIR | 3 | 8-200 | Yes |
| Brill et al. | SMATCH/FTIR | 23 | 100-350 | Yes |
| Brill and Brush | T-Jump FTIR | 16 | $\leq 2000$ | Yes |
| Behrens and Bulusu | Thermogravimetry/MBMS | 18 | 0.017 | Yes |
| Pesce-Rodriguez/Fifer | Pyrolysis/FTIR | 24 | 0.17 | Yes |
| Wormhoudt et al. | Strand Burning/IR Absorption | This Work | 10-100 | Yes |
| Wight and Botcher | Laser Heating/Cryotrap/FTIR | 25 | $1\text{-}3 \times 10^7$ | No |

# 7.0 SUMMARY

We draw three major conclusions from this work: $N_2O$ is observed as a decomposition product of RDX under actual propellant combustion conditions, it is formed in high temperature regions of the condensed phase and is able to penetrate into regions of the propellant which are otherwise little affected by the advancing flame front, and under our conditions its formation is not an initial step in RDX decomposition. Of course our observations by themselves will not fully specify the structure of a burning strand and the physical mechanisms which lie behind it, but they certainly strongly encourage the speculation that the suddenly appearing $N_2O$ originates in pressurized bubbles inside liquid RDX which in turn is contained inside a matrix formed by the propellant binder. This matrix would have to be structurally sound enough that some bubbles are prevented from releasing their contents upward into the flame region, but instead eject decomposition gas into the observation volume when cracks open creating vent paths.

# 8.0 REFERENCES

1.  M.H. Alexander, P.J. Dagdigian, M.E. Jacox, C.E. Kolb, C.F. Melius, H. Rabitz, M.D. Smooke, and W. Tsang, Prog. Energy Combust. Sci. 17, 263 (1991).

2.  G.F. Adams and R.W. Shaw, Jr., Ann. Rev. Phys. Chem. 43, 311 (1992).

3.  R.J. Karpowicz and T.B. Brill, Comb. Flame 56, 317 (1984).

4.  Y. Oyumi and T.B. Brill, Comb. Flame 62, 213 (1985).

5.  P.J. Miller, G.J. Piermarini, and S. Block, Appl. Spectrosc. 38, 680 (1984).

6.  P.J. Miller, S. Block and G.J. Piermarini, Comb. Flame 83, 174 (1991).

7.  J.P. Toscano and M. McBride, in ONR/LANL Workshop on the Fundamental Physics and Chemistry of Combustion, Initiation, and Detonation of Enegetic Materials, CPIA Publication 589, The Johns Hopkins University, March 1992, p. 71.

8.  T.B. Brill, Prog. Energy and Comb. Sci. 18, 91 (1992).

9.  M. Miller, 26th JANNAF Combustion Proceedings, CPIA Publication No. 529, Vol. III, 1989, p. 343.

10. K.L. Erickson, W. M. Trott, and A.M. Renlund, "Use of Thin-Film Samples to Study Thermal Decomposition of Explosives", paper presented at 18th International Pyrotechnics Seminar, Breckenridge, CO, 13-17 July, 1992.

11. B.L. Fetherolf and T.A. Litzinger, The Pennsylvania State University, private communication, 1992.

12. L.S. Rothman, R.R. Gamache, R.H. Tipping, C.P. Rinsland, M.A.H. Smith, D.C. Benner, V. Malathy Devi, J.-M. Flaud, C. Camy-Peyret, A. Perrin, A. Goldman, S.T. Massie, L. R. Brown and R. A. Toth, J. Quant. Spectrosc. Radiat. Transfer 48, 469 (1992).

13. R. Klein, M. Mentser, G. von Elbe, and B. Lewis, J. Phys. Colloid. Chem. 54, 877 (1950).

14. M. Miller, U. S. Army Research Laboratory, Aberdeen Proving Ground, private communication, 1993.

15. W.H. Hsieh, W. Y. Li and Y. J. Yim, AIAA Paper 92-3628, presented at AIAA/SAE/ASME/ASEE 28th Joint Propulsion Conference, July 6-8, 1992

16. T.B. Brill and P.J. Brush, Phil. Trans. R. Soc. Lond. A 339, 377 (1992).

17. Melius, C. F., 25th JANNAF Combustion Proceedings, CPIA Publication 498, Vol. II, 1988, p.155.

18. R. Behrens, Jr. and S. Bulusu, J. Phys. Chem. 96, 8877 (1992).

19. C.F. Melius, 25th JANNAF Combustion Proceedings, CPIA Publication 498, Vol. II, 1988, p. 155.

20. C.F. Melius, in Chemistry and Physics of Energetic Materials, Ed. S. Bulusu. ASI 309, NATO. p. 51.

21. L. Huwei and F. Ruonong, Thermochimica Acta 138, 167 (1989).

22. M.A. Schroeder, R. A. Fifer, M. S. Miller and R. A. Pesce-Rodriguez, BRL-MR-3845, Ballistic Research Laboratory, Aberdeen Proving Ground, MD, June 1990.

23. T.B. Brill, in Chemistry and Physics of Energetic Materials, Ed. S. Bulusu. ASI 309, NATO. p. 255.

24. R.A. Pesce-Rodriguez and R.A. Fifer, Pure & Appl. Chem. 65, 317 (1993).

25. C.A. Wight and T. R. Botcher, J. Am. Chem. Soc. 114, 8303 (1992).

26. T.R. Botcher and C.A. Wight, in Structure and Properties of Energetic Materials, Ed. D. H. Liebenberg, R. W. Armstrong, and J. J. Gilman, Mat. Res. Soc. Symp. Proc. 296, 47 (1993).

27. T.R. Botcher and C.A. Wight, J. Phys. Chem. 97, 9149 (1993).

28. C.F. Melius, in Chemistry and Physics of Energetic Materials, Ed. S. Bulusu. ASI 309, NATO. p. 21.

29. R. Behrens, Jr. and S. Bulusu, J. Phys. Chem. 96, 8891 (1992).

30. S.A. Shackelford, S.L. Rodgers, and R.E. Askins, Propellants, Explosives and Pyrotechnics 16, 279 (1991).

31. S.A. Shackelford, in Chemistry and Physics of Energetic Materials, Ed. S. Bulusu. ASI 309, NATO. p. 413.

32. X. Zhao, E.J. Hintsa and Y.T. Lee, J. Chem. Phys. 88, 801 (1988).

# 9.0 LIST OF PUBLICATIONS AND TECHNICAL REPORTS

"Infrared Fiber Optic Diagnostic for Solid Propellant Combustion," J. Wormhoudt and P.L. Kebabian, in Structure and properties of Energetic Materials, Materials Research Society Symposium Proceedings Vol. 296, Eds. D.H. Liebenberg, R.W. Armstrong and J.J. Gilman, Materials Research Society, Pittsburgh, PA, 1993, p. 367.

"Infrared Fiber Optic Diagnostic for Solid Propellant Combustion," J. Wormhoudt and P.L. Kebabian, 29th JANNAF Combustion Proceedings, CPIA Publication 593, Vol. 2, 1992, p. 263.

"Infrared Fiber Optic Diagnostic Observations of Solid Propellant Combustion," J. Wormhoudt and P.L. Kebabian, and C.E. Kolb, to be submitted to Combustion and Flame.

## 10. LIST OF PARTICIPATING SCIENTIFIC PERSONNEL

Dr. Charles E. Kolb was the Principal Investigator for the project. Dr. Joda Wormhoudt supervised the observations and reduced the data, and Dr. Paul Kebabian assisted with experiment design, construction, and testing.

Mr. Warren E. Goodwin constructed all the apparatus and test articles, and assisted in the observations.

## 11. REPORT OF INVENTIONS

This project did not result in any inventions, and we do not anticipate any patent application based on contract work.